DOI: https://doi.org/10.2138/am-2022-8260. http://www.minsocam.org/

Revision 3

Word Count: 7559

Nb and Ta intracrustal differentiation during granulite-facies metamorphism: evidence from geochemical data of natural rocks and thermodynamic modeling

Guangyu Huang[1,*], Yi Chen[1,*], Jinghui Guo[1], Richard Palin[2], Lei Zhao[1]

[1] State Key Laboratory of Lithospheric Evolution, Institute of Geology and Geophysics, Chinese Academy of Sciences, Beijing 100029, China

[2] Department of Earth Sciences, University of Oxford, Oxford, OX1 3AN, United Kingdom

*Corresponding author: Guangyu Huang (huangguangyu@mail.iggcas.ac.cn);

Yi Chen (chenyi@mail.iggcas.ac.cn)

ORCID: Guangyu Huang: http://orcid.org/0000-0002-2062-8095;

Yi Chen: http://orcid.org/0000-0001-6167-8032

ABSTRACT

Both continental crust and depleted mantle are characterized by subchondritic Nb/Ta, leading to a mass imbalance when compared to the bulk Earth. Even though several potential high Nb/Ta reservoirs in Earth's core and undepleted mantle have been proposed, little attention has been given to those in the crust. Here we present bulk-rock and rutile geochemical data for samples from a lower crustal pelitic granulite, North China Craton, which exhibit systematic variation in their Nb and Ta contents. High-temperature (HT) and ultra-high temperature (UHT) granulite residues exhibit Nb/Ta ratios that are close to chondritic and subchondritic, respectively, whereas leucosomes from UHT granulite mostly have suprachondritic Nb/Ta. These variations are best explained via competition for Nb and Ta between biotite and rutile during metamorphism, although initial bulk-rock Nb/Ta values also have an effect. As biotite preferentially incorporates Nb over Ta, the early stages of biotite dehydration melting produce a high-Nb/Ta residue and a low-Nb/Ta melt; however, geochemical modeling suggests that once biotite is depleted, the Nb/Ta ratio of the system is instead controlled by rutile growth, which promotes formation of a lower Nb/Ta residue and a higher Nb/Ta melt, even though the volume of melt produced at this stage may be small. We propose that *in-situ* and *in-source* leucosomes and leucocractic veins in UHT terranes may retain a high Nb/Ta geochemical signature. However, residual crustal-derived A2-type granites that experience significant fractionation of Nb- or Ta-bearing minerals during crystallization or contamination from other low-Nb/Ta sources cannot retain this high Nb/Ta ratio, even though these ratios are generally higher than that of S-type granites. Anhydrous partial melting of metapelite can generate Nb-rich melts, such that high temperature leucosomes in addition to related A2-type granites may represent significant Nb deposits.

Keywords: Nb/Ta; granulite; partial melting; forward modeling; ultra-high temperature; rutile

DOI: https://doi.org/10.2138/am-2022-8260. http://www.minsocam.org/

INTRODUCTION

Although the continental crust constitutes only ~0.6% mass of the silicate Earth, it contains a very large proportion of incompatible elements, which makes it a critical reservoir for mass-balance calculations of the Earth as a whole (Sclater et al., 1980). Previous studies have shown that both continental crust and depleted mantle have subchondritic Nb/Ta (Rudnick, 1995; Kelemen, 1995; Rudnick et al., 2000), which is problematic for chondritic Earth models, since no complementary suprachondritic Nb/Ta reservoirs are known. Although intracrustal Nb/Ta differentiation has received relatively little attention, several high Nb/Ta domains have been proposed to exist within the Earth to address this issue. These include the core, the lower mantle, the carbonatite-metasomatized lithospheric mantle, refractory eclogite formed during slab melting, and deeply crystalized high-Nb cumulates (Aulbach et al., 2008; Cartier et al., 2014; Münker et al., 2003; Pfänder et al., 2012; Rudnick et al., 2000; Tang et al., 2019; Wade and Wood, 2001; Willbold and Stracke, 2006). Recently, Stepanov and Hermann (2013) suggested that significant partial melting of restitic lower crust could produce a potential high-Nb and high Nb/Ta reservoir. In their model, incipient partial melting of mica-rich rocks during prograde metamorphism after muscovite incongruent melting ends, but before biotite dehydration melting begins, will produce a biotite-rich residue. Given that biotite incorporates Nb over Ta, the residue will evolve towards high Nb/Ta values during melt extraction. Progressive biotite-dehydration melting would then produce high-Nb/Ta rutile and ilmenite, since the D_{Nb}/D_{Ta} of rutile and ilmenite are close to unity. Nonetheless, experimental work performed by Xiong et al. (2011) showed that D_{Nb}/D_{Ta} of rutile and ilmenite at conditions relevant to biotite dehydration melting (850 °C) is approximately 0.8, and would be even lower during fluid-absent melting (Klemme et al., 2005; Xiong et al., 2011). Partition coefficients for Nb and Ta in different minerals are highly variable, and each is sensitive to pressure (*P*), temperature (*T*), and melt composition (Klemme et al., 2005; Xiong et al., 2011). Thus, understanding the behavior of these elements in the crust can place critical constraints on the mechanisms of intracrustal differentiation.

High-grade metamorphism and anatexis are ubiquitous in the lower crust, and melts that subsequently ascend through the overlying rock column and crystallize as granite at shallower depths represent a key mass-transfer process that leads to geochemical differentiation (Brown et al., 2011). During isobaric heating at pressures greater than ~0.5 GPa, such as during burial or crustal thickening, metapelites experience continuous partial melting as temperature increases, and biotite undergoes incongruent melting to form peritectic garnet and rutile (Sawyer et al., 2011; Patiño-Douce et al., 1991; Stevens et al., 2007). As a restitic phase, rutile is a major host for high field strength elements (HFSE) and act as a reservoir for the vast majority of Nb and Ta in a rock (Meinhold, 2010). Therefore, a detailed study of bulk-rock and rutile geochemistry in pelitic granulites is critical to decipher the evolution of the continental crust and develop small- and large-scale reservoir models.

In this study, a series of high-temperature (HT) to ultrahigh temperature (UHT) pelitic granulites from the northwestern part of the North China Craton were selected for a bulk-rock and rutile geochemical study. These data are compared to the results from petrological forward modeling for a typical metapelite that combines phase diagram analysis, accessory mineral solubility modeling, and trace element modeling. Integration of geochemical data from the study area with data for other granulites preserved worldwide allow Nb-Ta intracrustal geochemical fractionation processes during granulite-facies metamorphism to be further understood.

GEOLOGICAL SETTING

To explore Nb and Ta intracrustal geochemical fractionation processes during progressive heating, we studied several samples of granulite that share a common protolith, but record different thermal evolutions. These comprised pelitic granulites from the northern part of the Trans-North China Orogen and eastern part of the Khondalite Belt, North China Craton (Fig. 1a). The HT-HP granulites from the Trans-North China Orogen have been well-studied since the 2000s and UHT granulites in the Khondalite Belt contain well-preserved mineral assemblages diagnostic of peak metamorphic temperatures above 900 °C (Guo et al., 2002; Santosh et al., 2012). The Trans-North China Orogen is a north-south trending Paleoproterozoic orogenic belt (ca. 1.93–1.80 Ga) that separates the Eastern Block and Western Block of the North China Craton (Zhao et al., 2005). The northern part of the Trans-North China Orogen is dominated by tonalite–trondhjemite–granodiorite (TTG) and diorite gneisses that were emplaced at ca. 2.5 Ga, and that were metamorphosed at ca. 1.85 Ga. (Liu et al., 2012). Mafic granulite occurs as lenticular enclaves within the TTG gneisses, and metapelitic layers adjacent to the TTG gneisses record peak metamorphism at 1.92–1.85 Ga and *P*–*T* conditions of 1.1–1.2 GPa at temperatures < 900 °C, followed by decompression and cooling to the solidus (Huang et al., 2018; Wu et al., 2016). Additionally, HT-HP pelitic granulites have also been recognized in the Manjinggou and Huangtuyao areas (Wang et al., 2016; Wu et al., 2016; Zhang et al., 2016) (Fig. 1b).

Based on the subdivision by Zhao et al. (2005), the Western Block is divided into the Yinshan Block in the north and the Ordos Block in the south (Fig. 1a). The Khondalite Belt is an east-west trending Paleoproterozoic orogen, formed by the collision of the Yinshan Block and Ordos Block at ca. 1.95 Ga (Zhao et al., 2005). The eastern Khondalite Belt is dominated by aluminous gneiss, garnet-bearing orthogneiss, and minor gabbro and norite (Fig. 1b). UHT granulites with the diagnostic mineral assemblage sapphirine + quartz, initially recognized at the Tuguiwula area, record an initial stage of isobaric cooling from peak *P–T* conditions of 0.8–0.9 GPa at temperatures > 960 °C, followed by decompression and cooling to the solidus (Huang et al., 2019; Li and Wei, 2018; Santosh et al., 2012). UHT metamorphism has since been recognized from other localities, such as Heling'er, Xiaoshizi, and Zhaojiayao, indicating that heating was widespread in the eastern part of the Khondalite Belt (Jiao et al., 2013; Li et al., 2016; Liu et al., 2012). The garnet-bearing orthogneiss is peraluminous in composition and was emplaced at 1.95–1.94 Ga (Huang et al., 2019; Peng et al., 2012; Wang et al., 2018). This garnet-bearing orthogneiss and associated aluminous gneiss then experienced UHT metamorphism at ca. 1.92 Ga, which was likely induced by emplacement of nearby mafic magmas (Huang et al., 2019; Peng et al., 2010; Santosh et al., 2012). Given the belt-like distribution with small-scale and arc-like geochemical affinities, Peng et al. (2010) suggested that the mafic magmas are associated with a northwestward ridge-subduction-related mantle upwelling event.

SAMPLE DESCRIPTION

HT–HP granulite from the Trans-North China Orogen

Pelitic granulites from the Manjinggou area (Fig. 2a), northern Trans-North China Orogen, occur as layers adjacent to the TTG gneiss (Wu et al., 2016). *In-situ* to *in-source* leucosomes recognized in this area are interpreted as products of the crystallization of anatectic melts that have not migrated away from their source (Sawyer, 2008) (Fig. 2b). Minor syn-metamorphic S-type granite has been reported in this area. Given the relatively hot conditions of peak metamorphism (~ 850 °C) recorded by the metapelitic rocks, a significant amount of melt (up to 22 vol.%) should have been generated during heating (Huang et al., 2021); however, this amount is not observed in the field. Melts generated during metapelite partial melting are expected to dominantly ascend and collect in the upper crust to form granitic plutons (Brown, 2013). Therefore, the paucity of syn-metamorphic granite could be explained by the erosion of the overlying upper crustal levels during exhumation. The leucosomes have a simple mineralogy dominated by felsic minerals (i.e. plagioclase, K-feldspar and quartz), and were likely derived from biotite dehydration melting (Wu et al., 2016). Ten granulite samples (restite), collected from the Manjinggou area (Fig. 1b), contain K-feldspar, quartz, plagioclase, garnet, sillimanite, biotite, rutile, and minor kyanite (Fig. 3a, b). Accessory minerals include zircon, monazite, and apatite. In this study, detailed petrological work was conducted on sample 18MJ09 (GPS: 40°22′43.266″N, 114°27′56.404″E).

Garnet in sample 18MJ09 usually occurs as coarse-grained poikiloblasts that contain many small inclusions of quartz and/or biotite in the core domains (Fig. 3c). These inclusions, along with the garnet core itself, represent part of the prograde mineral assemblage (M_0). Kyanite is occasionally present as inclusions in the garnet rims (Fig. 3a, b), but not in the matrix. Biotite, K-feldspar, plagioclase, quartz, and rutile, that occur as inclusions with kyanite in garnet rims, define the peak pressure mineral assemblage (M_1). A key melt-forming prograde metamorphic reaction ($M_0 \rightarrow M_1$) is thus proposed to be biotite + quartz + plagioclase → garnet + kyanite + K-feldspar + melt (Wu et al., 2016). Rutile inclusions within garnet are either isolated or occur in spatial association with quartz and/or biotite (Fig. 3c, d). In the matrix, K-feldspar, plagioclase, quartz, sillimanite, garnet, biotite, and rutile represent a retrograde (decompressed) mineral assemblage (M_2). Thus, the polymorphic transition kyanite → sillimanite likely occurred during decompression (Wu et al., 2016). Rutile in the matrix occurs in contact with quartz, feldspar, garnet, and sillimanite.

UHT granulite from the eastern Khondalite Belt

Compared with HT granulite from northern Trans-North China Orogen, UHT granulite from the Tuguiwula area (Fig. 2c) in the eastern Khondalite Belt experienced more extensive partial melting (Fig. 2d). Alongside *in-situ* to *in-source* leucosomes, leucocratic veins were also recognized in the field and are interpreted as the product of crystallization of anatectic melts that migrated out of their source domain and were injected into adjacent rocks (Sawyer, 2008). Meanwhile, voluminous syn-metamorphic S-type granites, which compose 40 vol. % of the eastern Khondalite Belt, have been reported by many workers (e.g. Huang et al., 2019; Peng et al., 2012; Wang et al., 2018). The leucosomes mainly contain felsic minerals with minor garnet, sillimanite, and spinel. Given that few hydrous minerals remain in the residues and leucosomes, these leucosomes most likely crystallized from anhydrous melts. Fourteen felsic granulite samples (restites) and nine layered leucosomes in the granulite were collected from the Tuguiwula area. The sedimentary protoliths of these granulite samples varied lithologically between graywacke and pelite. Here, we focus on felsic paragneiss (restite) sample 16TG53 (GPS: 40°46′26.57″N, 113°11′4.05″E), which is a meta-graywacke (Fig. 2c), and contains plagioclase, quartz, K-feldspar, garnet, sillimanite, biotite, and rutile (Fig. 4). Accessory minerals include zircon, monazite, and apatite.

In sample 16TG53, sillimanite occurs only as inclusions in garnet – not in the matrix (Fig. 4a, c) – and so it is considered part of the prograde mineral assemblage (M_0). This assemblage additionally included plagioclase, K-feldspar, quartz, biotite, and rutile, as recorded by inclusions in garnet. Rutile inclusions in garnet occurs either as isolated grains or in association with quartz and/or biotite (Fig. 4). Coarse-grained garnet (>3 mm diameter), plagioclase, K-feldspar, quartz, and rutile in the matrix form the peak assemblage (M_1),

DOI: https://doi.org/10.2138/am-2022-8260. http://www.minsocam.org/

indicating progression of the prograde metamorphic reaction biotie + sillimanite → garnet + K-feldspar + rutile + melt. Rutile grains occur both in contact with felsic minerals and garnet (Fig. 4b, c, d). Coarse-grained matrix garnet and K-feldspar are locally separated by fine- to medium-grained biotite, sillimanite, and rutile (Fig. 4c, d), suggesting that K-feldspar, quartz, garnet, sillimanite, biotite, and rutile represent a retrograde mineral assemblage (M_2) that formed due to the reaction garnet + K-feldspar + rutile + melt → biotite + sillimanite.

METHODS

Analytical methods

Whole-rock major and trace elements.

Whole-rock major element compositions were determined by X-Ray fluorescence (XRF) at the State Key Laboratory of Lithospheric Evolution, Chinese Academy of Sciences, Beijing, China. The samples were crushed and powdered to 200 mesh using an agate mortar. Afterwards, approximately 0.50 g of rock powder was ignited at 1000 °C for ~1 hr to obtain loss on ignition (LOI) and then fused with three to four drops of lithium tetraborate using a CLAISSE M4 Fluxer. Uncertainties depend on the concentrations in the sample, but are generally better than ±1%.

Whole-rock trace element analyses were obtained at the China University of Geosciences (Wuhan). Rock powders were digested using a HF+HNO_3 solution in high-pressure Teflon bombs. Trace element concentrations were analyzed by inductively coupled plasma mass spectrometry (ICP-MS) using an Agilent 7700e system. The analytical precision and accuracy for trace element concentrations are described by Liu et al. (2008). The precision for most elements was typically better than ±5% RSD (relative standard deviation) calculated by analyses of repeated unknown samples and certified USGS reference materials (BHVO-2, BCR-2 and RGM-2) (USGS, 1996, 2004).

Electron probe microanalysis (EPMA).

Rutile compositions were analyzed via EPMA at the State Key Laboratory of Lithospheric Evolution, Institute of Geology and Geophysics, Chinese Academy of Sciences, Beijing, China (IGGCAS) using a CAMECA SX51. The microprobe employed an accelerating voltage of 20 kV, a beam current of 200 nA, and a beam diameter of 5 μm. The following elements were analyzed: Ti, V, Zr, Nb, Ta, Cr, Fe, Al, and Si. The counting time on the peak was 10 s, 120 s, 240 s, 120 s, 240 s, 120 s, 120 s, 120 s, and 240 s, respectively (Wang et al., 2017). The detection limits are 706 ppm for Ti, 84 ppm for V, 118 ppm for Zr, 144 ppm for Nb, 210 ppm for Ta, 154 ppm for Cr, 126 ppm for Fe, 60 ppm for Al, and 36 ppm for Si. Rutile R10 was used as a standard (Luvizotto et al., 2009b). Silicon concentrations were used as a quality control to detect and avoid contamination associated with submicroscopic zircon inclusions (Zack et al., 2004; Luvizotto et al., 2009a). Rutile measurements with Si contents higher than 300 ppm and those showing abnormal Ti concentrations were eliminated from the data set.

Laser-ablation quadrupole inductively coupled plasma mass spectrometry (LA-Q-ICP-MS).

Trace element analysis of rutile was conducted by LA-ICP-MS at the Wuhan SampleSolution Analytical Technology Co., Ltd., Wuhan, China. Detailed operating conditions for the laser ablation system and the ICP-MS instrument and data reduction are the same as those described by Zong et al. (2017). Laser sampling was performed using a GeolasPro laser ablation system that consists of a COMPexPro 102 ArF excimer laser (wavelength of 193 nm and maximum energy of 200 mJ) and a MicroLas optical system. An Agilent 7900 ICP-MS instrument was used to acquire ion-signal intensities. Helium was used as a carrier gas. Argon was used as the make-up gas and mixed with the carrier gas via a T-connector before entering the ICP. A "wire" signal smoothing device is included in this laser ablation system (Hu et al., 2015). The spot size and frequency of the laser were set to 44 μm and 5 Hz, respectively. Trace element compositions of minerals were calibrated against various reference materials (NIST 610, BHVO-2G, BCR-2G, and BIR-1G) without using an internal standard (Jochum et al., 2007, 2011; Liu et al., 2008; USGS, 1996, 2004). Each analysis incorporated a background acquisition of approximately 20-30 s followed by 50 s of data acquisition from the sample. The Excel-based software ICPMSDataCal was used to perform off-line selection and integration of background and analyzed signals, time-drift correction and quantitative calibration for trace element analysis (Liu et al., 2008). The mean values of uncertainties (2σ) and detection limits are 256 ppm and 1.09 ppm for V, 158 ppm and 1.24 ppm for Zr, 5.95 ppm, and 0.196 ppm for Hf, 94.6 ppm and 1.86 ppm for Nb, 6.57 ppm and 0.101 ppm for Ta, and 68.3 ppm and 12.8 ppm for Cr.

Modeling of partial melting of metapelite

Phase equilibria modeling.

Phase equilibria modeling was conducted on a typical metapelite (Ague, 1991) using THERMOCALC v. 3.40 (Powell and Holland, 1988) with internally consistent data set (ds62) of Holland and Powell (2011). The calculations were performed in the Na_2O-CaO-K_2O-FeO-MgO-Al_2O_3-SiO_2-H_2O-TiO_2-Fe_2O_3 chemical system using *a-x* models from White et al. (2014). Quartz, rutile, and H_2O were considered as pure phases. The H_2O content was assigned so that the modeled composition was minimally saturated at the solidus to ensure fluid-absent melting (cf. Palin et al., 2016a). The Fe^{3+}/Fe^{total} was constrained so that rutile was stable in the *P*–*T* range. Uncertainty on the position of the assemblage field boundaries is commonly less than ±50 °C and ±1 kbar at 2 σ. (Palin et al., 2016b).

Progressive partial melting in a rock would induce an interconnected network of grain-boundary melt-filled channels that allow its escape at a critical threshold (7 vol. %) in the absence of syn-anatectic deformation (Rosenberg and Handy, 2005). This threshold would be even lower in the presence of syn-anatectic deformation (Brown, 2010). We modeled melt loss events as realistically as possible by conducting thermodynamic modeling in a conditional open system (e.g. Yakymchuk and Brown, 2014). The critical melt connectivity threshold of 7 vol. % was used to model open-system processes, whereby once that proportion was reached along the proposed *P*–*T* paths of interest, six-sevenths of the melt present were removed as a 'melt loss event', based on the common observation of small proportions (1 vol.%) remaining of melts occurring as films on grain boundaries in rapid chilled and drained migmatites (Yakymchuk and Brown, 2014). In reality, this melt drainage process would represent a melt fraction that leaves the local system and ascends through the overlying crustal column towards the Earth's surface. This was performed during calculation by manipulation of the 'rbi' script, as outlined by Yakymchuk and Brown (2014). The compositions of extracted melt are listed in Table S4. Three thermal gradients including isobaric heating at 0.8 GPa, 775 °C/GPa, and 550 °C/GPa were selected to represent the overriding plate of a subduction zone, burial, and crustal thickening settings, respectively. A temperature of 640 °C, which is close to the wet-granite solidus and a good approximation of the starting point of partial melting (Yakymchuk and Brown, 2014), was selected as the lower boundary of the phase diagram.

Trace element modeling.

Trace element modeling was carried out using the batch melting equation $C_{melt}/C_{source} = 1/[D + F \times (1 - D)]$ (Shaw, 1970), where C_{source} and C_{melt} represent concentrations of a trace element in the source rock and the resultant melt, respectively; D (= $\sum$ Kd × X) is the bulk partition coefficient, where Kd is the mineral/melt partition coefficient and X is the proportion in mol. % of the mineral. F is the degree of melting. Initial bulk concentrations of 0.19 wt. % P_2O_5, 17 ppm Nb, 1.5 ppm Ta, 150 ppm Zr, and 150 ppm LREE were used for the metapelite (Taylor and McLennan, 1985; Ague, 1991; Yakymchuk et al., 2018). The proportions of accessory minerals in the residue were calculated using the refined zircon solubility model from Boehnke et al. (2013), the monazite solubility model from Stepanov et al. (2012), and the apatite solubility model from Harrison and Watson (1984). The Kd values used in the modeling are mostly mean values taken from the literature and tabulated in Table 1, except for rutile. As a peritectic phase from biotite dehydration melting, rutile will always be stable during granulite-facies metamorphism. However, the D_{Nb}/D_{Ta} of rutile decreases with temperature (Xiong et al., 2011), and would be around 0.8 at the conditions relevant to biotite dehydration melting (i.e. 850 °C) and approximately 0.45 in dry material at UHT conditions (Xiong et al., 2011; Klemme et al., 2005). In such cases, specific Kd values of rutile, used in the modeling, are listed in Table 1. The calculated Nb and Ta concentrations in the melts are listed in Table S4, and masses of accessory minerals left in the residue are listed in Table S5.

RESULTS

Bulk-rock composition of granulites and leucosomes

Granulites collected from the northern Trans-North China Orogen have mostly similar bulk-rock compositions, with SiO_2 = 53.2–68.4 wt.% (mean 62.7 wt.%), Al_2O_3 = 14.6–23.2 wt.% (mean 18.5 wt.%), and MgO = 2.1–3.4 wt.% (mean 2.6 wt.%). Heat-producing elements (e.g. K, Th, U) have consistent and relatively high concentrations (K_2O = 2.3–4.4 wt.%, U = 0.6–2.1 ppm, and Th = 10.4–18.6 ppm). Niobium concentrations range from 12.8 to 15.6 ppm, and Nb/Ta ratios vary from 16.9 to 24.8, with a mean of 20.5, which is slightly higher than the chondritic value of 19.9 (Fig. 5a) (Münker et al., 2003). By comparison, restites collected from the eastern Khondalite Belt have more variable SiO_2 (51.8–70.4 wt.%, mean 59.3 wt.%), higher Al_2O_3 (13.6–25.1 wt.%, mean 20.2 wt.%), and higher MgO (2.2–6.1 wt.%, mean 3.5 wt.%). The lower SiO_2 and higher Al_2O_3 and MgO concentrations likely resulted from significant melt loss (Lal et al., 1978; Clifford et al., 1981; Droop and Bucher-Nurminen, 1984; Raith et al., 1997; Baba, 2003; Brandt et al., 2007; Huang et al., 2021). Heat-producing elements usually show variable concentrations, but are more depleted than those in HT granulites (K_2O = 0.5–4.6 wt.%, U = 0.2–1.3 ppm, Th = 0.6–11.3 ppm). As discussed by Ewing et al. (2014), UHT metamorphism is an important process in driving the differentiation of the continental crust into an upper crust rich in heat-producing elements and a relatively depleted lower crust. Variability in heat-producing element concentrations in restites from the eastern Khondalite Belt likely relate to various degrees of partial melting. These UHT restites have Nb contents in the range 3.7–26.8 ppm and Nb/Ta ratios of 12.5–21.1, with a mean value of 16.8, which is lower than the chondritic value, but higher than that for a bulk continental crust (BCC) of 12.4 (Rudnick and Gao, 2014) (Fig. 5b). Conversely, leucosomes within these granulites, which represent anhydrous melts generated *in-situ* during UHT metamorphism, have a distinct bulk-rock composition from the restites. All the leucosomes are granitic and peraluminous, having SiO_2 contents in the range of 66.3–72.9 wt. %, and A/CNK [molar Al_2O_3/(CaO + Na_2O + K_2O)] values in the range of 1.3–2.4. These leucosomes have Nb contents of 0.4 ppm to 10.1 ppm, and Nb/Ta ratios of 17.1 to 44.1, with a mean of 24.1 (Fig. 6a).

Rutile trace elements

Rutile grains in HT-HP granulite sample 18MJ09 have Zr concentrations mostly ranging from 644 ppm to 2920 ppm (Fig. 7a). Based on the results of pressure-corrected Zr-in-rutile thermometry (Tomkins et al., 2007), sample 18MJ09 registered a peak temperature of 883 °C at a pressure of 1.1 GPa suggested by Wu et al. (2016). Specifically, Zr concentrations of isolated rutile inclusions in the matrix and rutile inclusions associated with quartz in garnet porphyroblasts cluster into two groups at 644–929 ppm and 2400–2920 ppm, of which the former group represents prograde growth and the latter represents growth at peak metamorphism. In the matrix, rutile in contact with felsic minerals or sillimanite usually has a high and restricted range of Zr concentrations (2560–2870 ppm), but those in contact with garnet have more variable Zr concentrations (1120–2620 ppm). Niobium concentrations in rutile are mostly 1320–2260 ppm, and Nb/Ta ratios are 16.3–32.6 with a mean value of 20.7 (Fig. 7a). Among those rutile grains, isolated rutile inclusions in garnet with high Zr concentrations have variable Nb/Ta ratios of 16.3–32.6, whereas others show limited variation (18.8–24.4). Figure 7a shows that rutile grains with high Nb/Ta usually have high Zr concentrations, indicating that they formed at higher temperatures, and so are inferred to have formed from a biotite-breakdown peritectic reaction (Fig. 7a).

Rutile in UHT granulite sample 16TG53 has Zr concentrations ranging from 314 to 6710 ppm (Fig. 7b), corresponding to temperatures of 645–980 °C at 0.80 GPa (cf. Huang et al., 2019). Among the various habits of rutile, isolated rutile inclusions and those associated with quartz in garnet porphyroblasts have the highest Zr concentrations. Most other rutile grains have relatively lower Zr concentrations, except for several that occur in contact with felsic minerals. Rutile in the matrix contains 607–3960 ppm Nb, with a mean of 2780 ppm, and Nb/Ta ratios range from 10.3 to 35.0 with a mean value of 17.5. Some individual rutile inclusions within garnet have much lower Nb concentrations (607–637 ppm) but higher Nb/Ta ratios (34.1–35.0). Some retrograde rutile grains around garnet have lower Zr concentrations (884–1160 ppm) but higher Nb/Ta ratios (38.6–64.7) (Fig. 7b).

Modeling results

Since melt produced during partial melting will leave its host rock when it reaches a critical melt connectivity transition (MCT) of 7 vol. % (Rosenberg and Handy, 2005), petrological modeling of equilibrium phase assemblages must take into account repeated melt loss and the production of an increasingly refractory residuum. Isobaric heating at 0.8 GPa from subsolidus conditions (700 °C) to UHT conditions (1000 °C) was used to simulate thermal metamorphism of the lower continental crust. At these conditions, five 'melt loss events' are predicted to occur at 754 °C, 780 °C, 808 °C, 828 °C, and 913 °C (Fig. 6b, 8). The first melt produced during metamorphism forms via muscovite-dehydration melting reactions, whereas melt generated between melt loss events 2 and 4 is produced by biotite-dehydration melting reactions. Melt lost during melt loss event 5 is generated via anhydrous breakdown of feldspar and quartz. All melt fractions show a progressive increase in A/CNK (1.12–1.21) with increasing temperature. Melts expelled during melt loss events 1–4 show increasing (but subchondritic)

DOI: https://doi.org/10.2138/am-2022-8260. http://www.minsocam.org/

Nb/Ta ratios of 4.91–15.0. The final melts to be generated and expelled have suprachondritic Nb/Ta ratios of 26.8, which is consistent with bulk compositions recorded by leucosomes in natural granulites (Fig. 6).

DISCUSSION

Intracrustal differentiation during granulite-facies metamorphism

Several episodes of partial melting are known to occur in felsic rock types during prograde metamorphism, which are driven by the breakdown of various hydrous and anhydrous minerals (Brown, 2013; Sawyer et al., 2011). Loss of melt from these host rocks and its vertical ascent to shallower levels induces intracrustal differentiation, which is the main form of mass transfer that controls the evolution of the continental crust through geological time (Brown et al., 2011; Palin and Santosh, 2021).

Fluid-present melting may occur in pelitic rocks at temperatures as low as ~650 °C due to simultaneous consumption of grain-boundary fluid and anhydrous felsic minerals (Sawyer et al., 2011). Thus, Nb-Ta fractionation may occur between the melt and residue during this process. However, as the main mineral hosts for Nb and Ta (i.e. muscovite, biotite, and oxide minerals) are not involved in these reactions, the Nb-Ta content and Nb/Ta of the residues will likely not change and the expelled melts will be Nb- and Ta-poor. Once free fluids are exhausted during heating, incongruent melting of hydrous minerals will occur, with muscovite- and biotite-breakdown reactions considered as the primary mechanism for generating crustal (S-type) granites (Brown, 2013; White et al., 2017). Partial melt in the source rock may generate substantial overpressure, leading to fracturing and so aiding subsequent melt loss (Clemens and Droop, 1998). Our modeling of isobaric heating at 0.8 GPa indicates that metapelites can lose up to 27 vol. % of their original mass via extraction of five discrete melt fractions (Fig. 8). The heat-producing element (U, Th and K) budget of the source will be progressively depleted, as the minerals hosting these elements, e.g. zircon, monazite and apatite, will progressively dissolve during partial melting and these elements will readily enter the silicate melt prior to its extraction (Rudnick and Gao, 2014; Ewing et al., 2014; Huang et al., 2021). The HT granulites studied here show limited depletion in heat-producing element concentrations, which indicates only a relatively minor degree of partial melting and melt loss compared to those that reached UHT conditions. The bulk rock Nb/Ta ratio at this stage is thus mainly controlled by muscovite and biotite stability, since mica is ubiquitous, but peritectic rutile is scarce. As biotite preferentially incorporates Nb over Ta (Stepanov and Hermann, 2013), anatexis would produce a restite with a high Nb/Ta ratio and melt with a low Nb/Ta ratio (Fig. 5a, 6b). However, the amount of biotite in the restite will decrease during heating, as it is consumed during melt-producing reactions. As such, the Nb/Ta budget of the residue will instead be controlled by rutile and ilmenite once biotite is scarce. After biotite is totally consumed at about 840 °C, the restites show a strong depletion in heat-producing elements, since U and Th host minerals (e.g. zircon, monazite and apatite) are mostly dissolved along with biotite (e.g. Ewing et al., 2014; Huang et al., 2021). The UHT residues in this study usually show clear depletion in heat-producing elements, indicating substantial partial melting and melt loss. During anhydrous melting, the rate of melt production is predicted to dramatically decrease (Sawyer et al., 2011), but this process will generate a relatively low Nb/Ta restite and high Nb/Ta melt (Fig. 5b, 6), since rutile is the main host mineral and preferentially incorporates Ta over Nb under anhydrous melting conditions (Klemme et al., 2005, Xiong et al., 2011).

Rutile in both samples shows a bimodal distribution of Zr concentrations, which is consistent with data reported previously by Luvizotto et al. (2009a). In that study, they proposed that the highest Zr contents recorded peak temperatures; as such, peak metamorphism in the two samples studied here would be 880 °C for 18MJ09 and 980 °C for 16TG53, which is consistent with phase equilibria modeling results (Wu et al., 2016; Huang et al., 2019). Biotite was stable during each metamorphic stage in sample 18MJ09 and rutile preserves variable Nb/Ta values. However, most rutile in UHT granulite sample 16TG53 has a narrow range of subchondritic Nb/Ta values and controls the bulk-rock Nb/Ta ratio (Fig. 8). From these patterns, it can be deduced that biotite breakdown during HT granulite-facies metamorphism caused variability in rutile Nb/Ta ratios. However, continued metamorphism and melting at UHT conditions, where biotite is no longer stable, leads to the continuous dynamic recrystallization of rutile, which is the only Nb- and Ta- carrier in the residue. This in turn causes the Nb/Ta ratio to evolve towards an equilibrium value (Luzizotto et al., 2009a). However, several rutile inclusions within garnet and retrograde rutile grains around garnet have much higher Nb/Ta values than the majority. Among these, high Nb/Ta isolated rutile inclusions in garnet have Cr/Nb > 1, which indicates that they may be rutile sourced from a metamafic rock (Meinhold, 2010). Since Nb and Ta are strongly incompatible in garnet, the Nb and Ta concentrations of these isolated rutile inclusions in garnet could be preserved even during UHT metamorphism (Fulmer et al., 2010). In such cases, these isolated rutile inclusions in garnet are most likely inherited rutile derived from eroded mafic rocks (Meinhold, 2010). Retrograde rutile grains with high Nb/Ta ratios are predicted to have formed alongside garnet, biotite, K-feldspar, and high Nb/Ta melts.

Nb/Ta of extracted melt along various geothermal gradients

To further explore Nb/Ta geochemical fractionation during granulite-facies metamorphism in different tectonic settings, geochemical modeling was also performed along two additional geothermal gradients for comparison with the isobaric heating path discussed above. These gradients were 775 °C/GPa and 550 °C/GPa, with the former considered as the lower threshold of the high d*T*/d*P* field representing UHT metamorphism (e.g. Brown and Johnson, 2018), and the latter representing a typical intermediate d*T*/d*P* thermal gradient passing through the high-pressure granulite facies field (O'Brien and Rötzler, 2003; Palin et al., 2020). *P*–*T* pseudosections and changing mineral proportions during heating are shown in the Supplementary Files. The modeling results for Nb/Ta from extracted melt against temperature are shown in Figure 9.

Four melt loss events are predicted to occur before 1000 °C along a thermal gradient of 775 °C/GPa (Fig. 9b). Given that five similar melt loss events are predicted during isobaric heating at 0.8 GPa, collisional tectonic processes appear to reduce the fertility of rocks more effectively than static heating (e.g. Yakymchuk and Brown, 2014). The extracted melts generated during melt loss events 1 to 4 for 775 °C/GPa have subchondritic Nb/Ta values of 6.75–14.2, which are slightly higher than those for corresponding melts generated at melt loss events 1 to 4 during isobaric heating at 0.8 GPa (Fig. 9a, b), as more rutile is stable during metamorphism at a thermal gradient of 775 °C/GPa. It is notable that the melt produced at UHT conditions would also have a suprachondritic Nb/Ta ratio (24.1), even though no melt loss events would occur.

Along a thermal gradient of 550 °C/GPa, eight melt loss events would occur up to 1000 °C (Fig. 9c), caused by a much higher initial H_2O content in the metapelite needed to ensure minimal saturation at the solidus (cf. section 4.2.1). Specifically, melt generated at melt loss

DOI: https://doi.org/10.2138/am-2022-8260. http://www.minsocam.org/

events 4 to 8 (in the short interval 988–992 °C) is formed via muscovite-dehydration melting. The Nb/Ta ratios of these melts show a systematic increase upon heating. However, no suprachondritic melt is generated along such a lower thermal gradient (7.90–13.7), since muscovite preferentially incorporates Nb over Ta (Raimbault and Burnol, 1998; Stepanov and Hermann, 2013), and remains stable up to 992 °C.

These data suggest that melt generated and lost sequentially during metamorphism will progressively evolve toward high Nb/Ta values upon heating, irrespective of the thermal gradients. However, we predict that the range of Nb/Ta values of extracted melts will be greater at higher thermal gradients (i.e. 4.9–26.8 during isobaric heating at 0.8 GPa) compared to low thermal gradients (i.e. 7.9–13.7 along 550 °C/GPa). Higher thermal gradient thus leads the crust to become more geochemically differentiated in terms of Nb-Ta systematics.

IMPLICATIONS

Figure 10 summarizes measured Nb/Ta values for typical HT (peak temperature < 900 °C) and UHT granulites, including well-studied examples from the Ivrea Verbano zone, northern Italy, and the Napier complex, Antarctic (Ewing et al., 2014; Grew et al., 2006). Although both HT and UHT granulite extend over wide Nb/Ta ranges, HT granulites usually have higher Nb/Ta values than UHT granulites, with average Nb/Ta values in HT granulites being close to chondritic, and those in UHT granulites being subchondritic. Since most granulites have Nb contents clustering in the range 0–40 ppm, the difference of Nb/Ta values comes from having higher Ta contents within UHT granulites than those of HT granulites (Fig. 5, S5). Further, as most low-grade argillaceous sediments have low Nb/Ta values (mean = 11.0, Taylor and McLennan, 1985), we suggest that the Nb/Ta value of a metapelite would show a bell-shaped evolution during prograde heating, including progressive increase and decrease of Nb/Ta ratios during low and high temperature melting, respectively. The modeling results in this study qualitatively show this trend, but no suprachonditic Nb/Ta values were reproduced in the residues of partial melting (Fig. 9). This is inconsistent with natural samples, as HT granulites have previously been proposed as a high Nb/Ta reservoir (Stepanov and Hermann, 2013). One possible reason for this mismatch is that protoliths have different TiO_2 contents; for example, all the granulites considered here have less than 1.0 wt.% TiO_2, and all HT granulites have an average TiO_2 content of 0.79 wt.%. However, the TiO_2 content of the protolith used for modeling was 1.06 wt.%, and melt extraction lead to an increase in residual TiO_2 contents of up to 1.30–1.63 wt.% (i.e., two-time higher than those of HT granulites) (Table S3, S4). Higher bulk-rock TiO_2 contents can stabilize more rutile in the residue, potentially leading to lower Nb/Ta after melt loss.

Leucosomes in UHT terranes are thought to have crystallized from melt derived from *in-situ* anatexis of their host rocks, and usually have a high Nb/Ta ratio (up to 44). By using the Nb and Ta contents of rutile in granulites and rutile/melt partition coefficient, the calculated melts in equilibrium with UHT-stage rutile would have Nb contents up to 71.5 ppm, and Nb/Ta values up to 42 (Fig. 11). For the same UHT sample (16TG53), calculated melts in equilibrium with prograde-stage rutile (M_0) would have lower Nb contents and Nb/Ta (up to 22 ppm and 22, respectively). For the HT granulite (18TG09), calculated melts would have a Nb content below 14 ppm, but suprachondritic Nb/Ta value in the range of 20–40 (Fig. 11). However, muscovite-bearing peraluminous granite samples compiled by Ballouard et al. (2020), that were interpreted to be derived from segregation, ascent, and emplacement of relatively low-temperature melts generated by muscovite dehydration, have low Nb/Ta values in the range 5–15 (mean = 6.86) (Fig. 6a). Highly differentiated muscovite-bearing peraluminous granites, that experienced significant magmatic-hydrothermal alteration, have Nb/Ta < 5 (Ballouard et al., 2016), and were excluded from the compilation. Our modeling results for partial melting of an average pelite also show a monotonous Nb/Ta increase in melt extracted during heating, which is similar to that of natural samples (Fig. 6b, 9).

Given that the Nb/Ta ratio of natural leucosomes in the UHT terrane and calculated anhydrous melts at UHT condition are both suprachondritic, A2-type granite, which is derived from anatexis of dry refractory granulite residue (Collins et al., 1982; Eby, 1990, 1992; Ballouard et al., 2020), are expected to have a suprachondritic Nb/Ta ratio and potentially represent a relatively high Nb/Ta reservoir within the continental crust. Nonetheless, most A2-type granites are characterized by subchondritic Nb/Ta, even though they generally have higher Nb/Ta than highly peraluminous granites at given Nb and Ta contents (Ballouard et al., 2020) (Fig. 11). As discussed above, the melts generated by anhydrous melting can have suprachondritc Nb/Ta values, although natural processes associated with granite generation are often more complicated than the relatively simplistic model treatment applied above. Such natural complexity involves episodic melt production, melt extraction, mixing, differentiation, and emplacement (Clemens, 2012; Brown, 2013). High Nb/Ta minerals, such as biotite, may fractionate during any of these processes, leading to a decrease of Nb/Ta in the melt (Stepanov et al., 2014). In addition, magma mixing and contamination from other low Nb/Ta sources, such as a UHT residual mush, would also induce a chemical change in the melt during its ascent (e.g. Korhonen et al., 2015). Then, anhydrous melt, if unfractionated and lacking contamination, might retain a high Nb/Ta ratio, leading to *in-situ* leucosome, *in-source* leucosome, and some leucocractic veins in UHT terranes being potential high-Nb/Ta reservoirs.

We note that Nb and Ta intracrustal geochemical fractionation is important to both the "missing Nb paradox" that has implications for understanding whole-Earth geochemistry, but also to economic geology research into critical metal-bearing deposits. As important rare-metal elements, economic enrichments of Nb and Ta can be promoted by extreme degrees of fractional crystallization of assemblages comprising feldspar (over 90 %) from low-temperature S-type granite melts (Ballouard et al., 2016, 2020; Stepanov et al., 2014). Our petrological modeling results indicate that anhydrous melts produced in UHT terranes would have Nb contents mostly over 20 ppm, but potentially up to 71.5 ppm. Nonetheless, the Ta contents in these anhydrous melts would not be economically valuable, as rutile in the residual host retains too much Ta, leading to a subchondritic Nb/Ta in UHT granulites. A2-type granites appear to have a greater potential for retaining elevated Nb contents (Fig. 11) (Linnen and Cuney, 2005). We therefore propose that UHT melting of metapelite/metagraywacke may indeed represent an efficient process to produce high Nb and high Nb/Ta melts that may evolve and collect in the upper crust to form A2-type granites. Some of these granites may have the potential to form economic Nb deposits if they are significantly evolved and reach columbite saturation. High-T leucosomes from granulite terranes, representing frozen melts that did not migrated toward the upper crust, could theoretically represent a new, still undiscovered, type of Nb deposits.

ACKNOWLEDGMENTS

We specially acknowledge Christophe Ballouard for his four-time careful reviews and corrections. We are also grateful for reviews by Aleksandr Stepanov and an anonymous reviewer, and editorial comments from Antonio Acosta-Vigil and Daniel Harlov, which helped to improve the content and presentation of this article. We thank Qian Mao and Di Zhang for their help with EMPA analyses.

FUNDING

This work is financially supported by National Natural Science Foundation of China (grant No. 41890832, 41902057, 41822202 and 42172217) , Program of China-Sri Lanka Joint Center for Water Technology Research and Demonstration by the Chinese Academy of Sciences (CAS); China–Sri Lanka Joint Center for Education and Research by the CAS. The data used in this paper can be found in supplementary files.

REFERENCES CITED

Acosta-Vigil, A., Buick, I., Hermann, J., Cesare, B., Rubatto, D., London, D., and Morgan, G.B. (2010) Mechanisms of crustal anatexis: a geochemical study of partially melted metapelitic enclaves and host dacite, SE Spain. Journal of Petrology, 51, 785–821.

Ague, J.J. (1991) Evidence for major mass transfer and volume strain during regional metamorphism of pelites. Geology, 19, 855–858.

Aulbach, S., O'Reilly, S.Y., Griffin, W.L., and Pearson, N.J. (2008). Subcontinental lithospheric mantle origin of high niobium/tantalum ratios in eclogites. Nature Geoscience, 1, 468.

Auwera, J.V., Bogaerts, M., Liégeois, J.P., Demaiffe, D., Wilmart, E., Bolle, O., and Duchesne, J.C. (2003) Derivation of the 1.0–0.9 Ga ferro-potassic A-type granitoids of southern Norway by extreme differentiation from basic magmas. Precambrian Research, 124, 107–148.

Ballouard, C., Poujol, M., Boulvais, P., Branquet, Y., Tartèse, R., and Vigneresse, J.L. (2016) Nb-Ta fractionation in peraluminous granites: A marker of the magmatic-hydrothermal transition. Geology, 44, 231–234.

Ballouard, C., Massuyeau, M., Elburg, M.A., Tappe, S., Viljoen, F., and Brandenburg, J.-T. (2020) The magmatic and magmatic-hydrothermal evolution of felsic igneous rocks as seen through Nb-Ta geochemical fractionation, with implications for the origins of rare-metal mineralizations. Earth-Science Review, 203, 103115.

Bea, F., Pereira, M.D., and Stroh, A. (1994) Mineral/leucosome trace-element partitioning in a peraluminous migmatite (a laser ablation-ICP-MS study). Chemical Geology, 117, 291–312.

Boehnke, P., Watson, E.B., Trail, D., Harrison, T.M., and Schmitt, A.K. (2013) Zircon saturation re-revisited. Chemical Geology, 351, 324–334.

Brown, M., Korhonen, F.J., and Siddoway, C.S. (2011) Organizing melt flow through the crust. Elements, 7, 261–266.

Brown, M. (2013) Granite: From genesis to emplacement: Geological Society of America Bulletin, 125, 1079–1113.

Brown, M., and Johnson, T. (2018) Secular change in metamorphism and the onset of global plate tectonics. American Mineralogists, 103, 181–196.

Cai, J. (2014) Metamorphic Evolution and Geochronology of the Wulashan-Daqingshan Complex, the Khondalite Belt: PhD thesis (in Chinese with English abstract).

Cartier, C., Hammouda, T., Boyet, M., Bouhifd, M.A., and Devidal, J.-L. (2014) Redox control of the fractionation of niobium and tantalum during planetary accretion and core formation. Nature Geoscience, 7, 573.

Clemens, J.D., and Droop, G.T.R. (1998) Fluids, P–T paths and the fates of anatectic melts in the Earth's crust. Lithos, 44, 21–36.

Clemens, J.D., (2012) Granitic magmatism, from source to emplacement: a personal view. Applied Earth Science, 121(3), 107–136.

Clemens, J.D., and Stevens, G. (2016), Melt segregation and magma interactions during crustal melting: Breaking out of the matrix. Earth Science Review, 160, 333–349.

Collins, W., Beams, S., White, A., and Chappell, B. (1982) Nature and origin of A-type granites with particular reference to southeastern Australia. Contributions to Mineralogy and Petrology, 80, 189–200.

Eby, G.N., (1990) The A-type granitoids: a review of their occurrence and chemical characteristics and speculations on their petrogenesis. Lithos, 26, 115–134.

Eby, G.N., (1992) Chemical subdivision of the A-type granitoids:Petrogenetic and tectonic implications. Geology, 20, 641–644.

Ewing, T.A., Rubatto, D., and Hermann, J. (2014) Hafnium isotopes and Zr/Hf of rutile and zircon from lower crustal metapelites (Ivrea-Verbano Zone, Italy): Implications for chemical differentiation of the crust. Earth and Planetary Science Letter, 389, 106–118.

Fedele, L., Lustrino, M., Melluso, L., Morra, V., Zanetti, A., and Vannucci, R. (2015) Trace element partitioning between plagioclase, alkali feldspar, Ti-magnetite, biotite, apatite, and evolved potassic liquids from Campi Flegrei (Southern Italy). Ameircan Mineralogist, 100, 233–249.

Ferry, J.M., and Watson, E.B. (2007) New thermodynamic models and revised calibrations for the Ti-in-zircon and Zr-in-rutile thermometers. Contributions to Mineralogy and Petrology, 154, 429–437.

Fulmer, E.C., Nebel, O., and van Westrenen, W. (2010) High-precision high field strength element partitioning between garnet, amphibole and alkaline melt from Kakanui, New Zealand. Geochimica et Cosmochimica Acta, 74, 2741–2759.

Grew, E.S., Yates, M.G., Shearer, C.K., Hagerty, J.J., Sheraton, J.W., and Sandiford, M. (2006) Beryllium and Other Trace Elements in Paragneisses and Anatectic Veins of Ultrahigh-Temperature Napier Complex, Enderby Land, East Antarctica: the Role of Sapphirine. Journal of Petrology, 47, 859–882.

Guo, J.H., O'Brien, P.J., and Zhai, M.G. (2002) High-pressure granulites in the Sanggan area North China craton: metamorphic evolution, P–T paths and geotectonic significance. Journal of Metamorphic Geology, 20, 741–756.

Harrison, T.M., and Watson, E.B. (1984) The behavior of apatite during crustal anatexis: equilibrium and kinetic considerations. Geochimica et Cosmochimica Acta, 48, 1467–1477.

Holland, T.J.B., and Powell, R. (2011) An improved and extended internally consistent thermodynamic dataset for phases of petrological interest, involving a new equation of state for solids. Journal Metamorphic Geology, 29, 333–383.

Hu, Z.C., Zhang, W., Liu, Y.S., Gao, S., Li, M., Zong, K.Q., Chen, H.H., and Hu, S.H. (2015) "Wave" Signal-Smoothing and Mercury-Removing Device for Laser Ablation Quadrupole and Multiple Collector ICPMS Analysis: Application to Lead Isotope Analysis. Analytical Chemistry, 87(2), 1152–1157.

Huang, G.Y., Brown, M., Guo, J.H., Piccoli, P., and Zhang, D.D. (2018) Challenges in constraining the P–T conditions of mafic granulites: An example from the northern Trans-North China Orogen. Journal of Metamorphic Geology, 36, 739–768.

Huang, G.Y., Guo, J.H., Jiao, S.J., and Palin, R. (2019) What Drives the Continental Crust To Be Extremely Hot So Quickly? Journal of Geophysical Research: Solid Earth, 124, 11218–11231.

Huang, G.Y., Guo, J.H., and Palin, R. (2019) Phase equilibria modeling of anatexis during ultra-high temperature metamorphism of the crust. Lithos, 398–399, 106326.

Jiao, S. J., Guo, J.H., Harley, S.L., and Windley, B.F. (2013) New Constraints from Garnetite on the P-T Path of the Khondalite Belt: Implications for the Tectonic Evolution of the North China Craton. Journal of Petrology, 54(9), 1725–1758.

Jochum, K.P., Nohl, U., Herwig, K., Lammel, E., Stoll, B., and Hofmann, A.W. (2007) GeoReM: A New Geochemical Database for Reference Materials and Isotopic Standards. Geostandards and Geoanalytical Research, 29, 333–338.

Jochum, K.P., Weis, U., Stoll, B., Kuzmin, D., Yang, Q.C., Raczek, I., Jacob, D.E., Stracke, A., Birbaum, K., Frick, D.A., Gunther, D., and Enzweiler, J., (2011) Determination of Reference Values for NIST SRM 610-617 Glasses Following ISO Guidelines, Geostandards and Geoanalytical Research, 35, 397–429.

Kelemen, P.B. (1995) Genesis of high Mg# andesites and the continental crust. Contribution to Mineralogy and Petrology, 120, 1–19.

Kelsey, D.E., and Hand, M. (2015) On ultrahigh temperature crustal metamorphism: Phase equilibria, trace element thermometry, bulk composition, heat sources, timescales and tectonic settings. Geoscience Frontiers, 6, 311–356.

Klemme, S., Blundy, J.D., and Wood, B.J. (2002) Experimental constraints on major and trace element partitioning during partial melting of eclogite. Geochimica et Cosmochimica Acta, 66, 3109–3123.

Klemme, S., Prowatke, S., Hametner, K., and Gunther, D. (2005) Partitioning of trace elements between rutile and silicate melts: Implications for subduction zones. Geochimica et Cosmochimica Acta, 69, 2361–2371.

Klemme, S., Günther, D., Hametner, K., Prowatke, S., and Zack, T. (2006) The partitioning of trace elements between ilmenite, ulvospinel, armalcolite and silicate melts with implications for the early differentiation of the moon. Chemical Geology, 234, 251–263.

Korhonen, F., Brown, M., Clark, C., Foden, J.D., and Taylor, R. (2015) Are granites and granulites consanguineous? Geology, 43, 991–994.

Li, X.W., and Wei, C.J. (2018) Ultrahigh-temperature metamorphism in the Tuguiwula area, Khondalite Belt, North China Craton. Journal of Metamorphic Geology, 36, 489–509.

Li, X.W., and Wei, C.J. (2016) Phase equilibria modelling and zircon age dating of pelitic granulites in Zhaojiayao, from the Jining Group of the Khondalite Belt, North China Craon. Journal of Metamorphic Geology, 34, 595–615.

Liu, S.J., Tsunogae, T. Li, W.S., Shimizu, H., Santosh, M., Wan, Y.S., and Li, J.H. (2012) Paleoproterozoic granulites from Heling'er: Implications for regional ultra-high temperature metamorphism in the North China Craton. Lithos, 148, 54–70.

DOI: https://doi.org/10.2138/am-2022-8260. http://www.minsocam.org/

Linnen, R.L., and Cuney, M. (2005) Granite-related rare-element deposits and experimental constraints on Ta-Nb-W-Sn-Zr-Hf mineralization, in Linnen RL and Samson IM, eds., rare-element geochemistry and mineral deposits. In Geological Association of Canada, GAC, Short Course.

Linnen, R.L., and Keppler, H. (1997) Columbite solubility in granitic melts: consequences for the enrichment and fractionation of Nb and Ta in the Earth's crust. Contributions to Mineralogy and Petrology, 128, 213–227.

Liu, F., Guo, J. H., Peng, P., and Qian, Q. (2012) Zircon U-Pb ages and geochemistry of the Huai'an TTG gneisses terrane: Petrogenesis and implications for 2.5 Ga crustal growth in the North China Craton. Precambrian Research, 213, 225–244.

Liu, Y.S., Zong, K.Q., Kelemen, P.B., and Gao, S. (2008) Geochemistry and magmatic history of eclogites and ultramafic rocks from the Chinese continental scientific drill hole: Subduction and ultrahigh-pressure metamorphism of lower crustal cumulates. Chemical Geology, 247, 133–153.

Liu, Y.S., Gao, S., Hu, Z.C., Gao, C.G., Zong, K.Q., and Wang, D.B. (2010) Continental and Oceanic Crust Recycling-induced Melt-Peridotite Interactions in the Trans-North China Orogen: U-Pb Dating, Hf Isotopes and Trace Elements in Zircons from Mantle Xenoliths. Journal of Petrology, 51, 537–571.

Luvizotto, G.L., and Zack, T. (2009a) Nb and Zr behavior in rutile during high-grade metamorphism and retrogression: An example from the Ivrea-Verbano Zone. Chemical Geology, 261, 303–317.

Luvizotto, G.L., Zack, T., Meyer, H.P., Ludwig, T., Triebold, S., Kronz, A., Münker, C., Stockli, D.F., Prowatke, S., Klemme, S., Jacob, D.E., and von Eynatten, H. (2009b) Rutile crystals as potential trace element and isotope mineral standards for microanalysis. Chemical Geology, 261, 346–369.

Meinhold, G. (2010) Rutile and its applications in earth sciences. Earth Science Review, 102, 1–28.

Münker, C., Pfänder, J.A., Weyer, S., Büchl, A., Kleine, T., and Mezger, K. (2003) Evolution of planetary cores and the Earth-Moon system from Nb/Ta systematics. Science, 301, 84–87.

Nandakumar, V., and Harley, S.L. (2019) Geochemical signatures of mid-crustal melting processes and heat production in a hot orogen: The Kerala Khondalite Belt, Southern India. Lithos, 324–325, 479–500.

Nardi, L.V.S., Formoso, M.L.L., Müller, L.F., Fontana, E., Jarvis, K., and Lamarão, C. (2013) Zircon/rock partition coefficients of REEs, Y, Th, U, Nb, and Ta in granitic rocks: Uses for provenance and mineral exploration purposes. Chemical Geology, 335, 1–7.

Nash, W., and Crecraft, H. (1985) Partition coefficients for trace elements in silicic magmas. Geochimica et Cosmochimica Acta, 49, 2309–2322.

O'Brien, P.J. and Rötzler, J. (2003) High-pressure granulites: Formation, recovery of peak conditions and implications for tectonics. Journal of Metamorphic Geology, 21, 3–20.

Osanai, Y., Sajeev, K., Nakano, N., Kitano, I., Kehelpannala, W.K.V., Kato, R., Adachi, T., and Malaviarachchi, S.P.K. (2016a) UHT granulites of the Highland Complex, Sri Lanka I: Geological and petrological background. Journal of Mineralogical and Petrological Sciences 111, 145-156.

Osanai, Y., Sajeev, K., Nakano, N., Kitano, I., Kehelpannala, W.K.V., Kato, R., Adachi, T., and Malaviarachchi, S.P.K., (2016) UHT granulites of the Highland Complex, Sri Lanka II: Geochronological constraints and implications for Gondwana correlation. Journal of Mineralogical and Petrological Sciences, 111, 157-169.

Ouyang, D.J., Jinghui, Guo., Liou, P., and Huang, G. Y. (2019) Petrogenesis and tectonic implications of 2.45 Ga potassic A-type granite in the Daqingshan area, Yinshan Block, North China Craton. Precambrian Research, 336, 105435.

Palin, R.M. and Santosh, M. (2021). Plate tectonics: What, where, why, and when?. Gondwana Research, 100, 3-24.

Palin, R.M., White, R.W., Green, E.C.R., Diener, J.F., Powell, R., and Holland, T.J.B. (2016a) High - grade metamorphism and partial melting of basic and intermediate rocks. Journal of Metamorphic Geology, 34, 871–892.

Palin, R.M., Weller, O.M., Waters, D.J., and Dyck, B. (2016b) Quantifying geological uncertainty in metamorphic phase equilibria modelling; a Monte Carlo assessment and implications for tectonic interpretations. Geoscience Frontiers, 7, 591–607.

Palin, R.M., Santosh, M., Cao, W., Li, S.S., Hernández-Uribe, D. and Parsons, A. (2020) Secular change and the onset of plate tectonics on Earth. Earth-Science Reviews, 103172.

Pearce, N.J.G., Perkins, W.T., Westgate, J.A., Gorton, M.P., Jackson, S.E., Neal, C.R., and Chenery, S.P. (1997) A compilation of new and published major and trace element data for NIST SRM 610 and NIST SRM 612 glass reference materials. Geostandards and Geoanalytical Research, 21, 115–144.

Peng, P., Guo, J. H., Zhai, M., and Bleeker, W. (2010) Paleoproterozoic gabbronoritic and granitic magmatism in the northern margin of the North China craton: evidence of crustemantle interaction. Precambrian Research, 183, 635–659.

Peng, P., Guo, J.H., Windley, B.F., Liu, F., Chu, Z., and Zhai, M.G. (2012) Petrogenesis of Late Paleoproterozoic Liangcheng charnockites and S–type granites in the central northern margin of the North China Craton: implications for ridge subduction. Precambrian Research, 222–223, 107–123.

Pfänder, J.A., Jung, S., Münker, C., Stracke, A., and Mezger, K. (2012) A possible high Nb/Ta reservoir in the continental lithospheric mantle and consequences on the global Nb budget-Evidence from continental basalts from Central Germany. Geochimica et Cosmochimica Acta, 77, 232–251.

Powell, R., and Holland, T.J.B. (1988) An internally consistent dataset with uncertainties and correlations: 3. Applications to geobarometry, worked examples and a computer program. Journal Metamorphic Geology, 6, 173–204.

Prowatke, S., and Klemme, S. (2006) Trace element partitioning between apatite and silicate melts. Geochimica et Cosmochimica Acta, 70, 4513–4527.

Qian, Q., and Hermann, J. (2013) Partial melting of lower crust at 10-15 kbar: constraints on adakite and TTG formation. Contributions to Mineralogy and Petrology, 165, 1195–1224.

Raimbault, L., Cuney, M., Azencott, C., Duthou, J-L., and Joron, J.L. (1995) Geochemical evidence for a multistage magmatic genesis of Ta–Sn–Li mineralization in the granite at Beauvoir, French Massif Central. Economic Geology, 90, 548–576.

Raimbault, L., and Burnol, L. (1998) The Richemont rhyolite dyke, Massif Central, France; a subvolcanic equivalent of rare-metal granites. Canadian Mineralogist, 36, 265–282.

Rosenberg, C.L., and Handy, M.R. (2005) Experimental deformation of partially melted granite revisited: implications for the continental crust. Journal Metamorphic Geology, 23, 19–28.

Rudnick, R.L. (1995) Making continental crust. Nature, 378, 571–578.

Rudnick, R.L., Barth, M., Horn, I., and McDonough, W.F. (2000) Rutile-bearing refractory eclogites: missing link between continents and depleted mantle. Science, 287, 278–281.

Rudnick, R.L., and Gao, S. (2014) in Treatise on Geochemistry 2nd edn (eds Holland, H.D., and Turekian, K.K.), 1–51.

Santosh, M., Liu, S.J., Tsunogae, T., and Li, J.H. (2012) Paleoproterozoic ultrahigh–temperature granulites in the North China Craton: implications for tectonic models on extreme crustal metamorphism. Precambrian Research, 222–223, 77–106.

Sawyer, E.W., Cesare, B., and Brown, M. (2011) When the continental crust melts. Elements, 7, 229–234.

Sclater, J.G., Jaupart, C.J., and Galson, D. (1980) The heat flow through oceanic and continental crust and the heat loss of the earth. Review of Geophysics and Space Physics, 18, 269–311.

Shaw, D.M. (1970) Trace element fractionation during anatexis. Geochimica et Cosmochimica Acta, 34, 237–243.Sievwright, R.H., Wilkinson, J.J., O'Neill, H.S.C., and Berry, A.J. (2017) Thermodynamic controls on element partitioning between titanomagnetite and andesitic-dacitic silicate melts. Contributions to Mineralogy and Petrology, 172, 62.

Sizova, E., Gerya, T., and Brown, M. (2014) Contrasting styles of Phanerozoic and Precambrian continental collision. Gondwana Research, 25, 522–545.

Stepanov, A.S., Hermann, J., Rubatto, D., and Rapp, R.P. (2012) Experimental study of monazite/melt partitioning with implications for the REE, Th and U geochemistry of crustal rocks. Chemical Geology, 300, 200–220.

Stepanov, A.S., and Hermann, J. (2013) Fractionation of Nb and Ta by biotite and phengite: Implications for the “missing Nb paradox”. Geology, 41, 303–306.

Stepanov, A., Mavrogenes, J.A., Meffre, S., and Davidson, P. (2014) The key role of mica during igneous concentration of tantalum. Contributions to Mineralogy and Petrology, 167, 1009–1016.

Sun, S.S., and McDonough, W.F. (1989) Chemical and isotopic systematics of oceanic basalts: implications of mantle composition and processes. Geological Society London Special Publications, 42, 313–345.

Sweeney, R.J., Prozesky, V., and Przybylowicz, W. (1995) Selected trace and minor element partitioning between peridotite minerals and carbonatite melts at 18-46 kb pressure. Geochimica et Cosmochimica Acta, 59, 3671–3683.

Tang, M., Lee, C.T.A., Chen, K., Erdman, M., Cosin, G., and Jiang, H. (2019) Nb/Ta systematics in arc magma differentiation and the role of arclogites in continent formation. Nature Communication,10, 235.

Tomkins, H.S., Powell, R., and Ellis, D.J. (2007) The pressure dependence of the zirconium-in-rutile thermometer. Journal of Metamorphic Geology, 30, 235–254.

DOI: https://doi.org/10.2138/am-2022-8260. http://www.minsocam.org/

Taylor, S.R., and McLennan, S.M. (1985) The Continental Crust: Its composition and evolution. Oxford: Blackwell Scientific, p. 312.

USGS. (1996) Microbeam standard Columbia River basalt (Glass) BCR-2G, United States Geological Survey Special Bulletin (Reference Materials Project). US Geological Survey, report, 10pp.

USGS. (2004) Geochemical reference materials and certificates. http://minerals.cr.usgs.gov/geo_chem_stand/

Vansutre, S., Hari, K.R., and Vishwakarma, N. (2013) Implications of Geochemistry in support of Palaeo-Proterozoic Tectonothermal Evolution of Bhopalpatnam Granulite Belt, Bastar Craton, Central India. Journal of Geological Society of India, 81, 503–513.

Wang, J., Chen, Y., Mao, Q., Li, Q.L., Ma, Y.G., Shi,Y.H., and Song, C.Z. (2017) Electron microprobe trace element analysis of rutile. Acta Petrologica Sinica, 33, 1934–1946.

Wang, L.J., Guo, J.H., Yin, C.Q., Peng, P., Zhang, J., Spencere, C.J., and Qian, J.H. (2018) High–temperature S–type granitoids (charnockites) in the Jining Complex, North China Craton: resite entrainment and hybridization with maifc magma. Lithos, 320–321, 435–453.

Watson, E.B., Wark, D.A., andThomas, J.B. (2006) Crystallization thermometers for zircon and rutile. Contributions to Mineralogy and Petrology, 151, 413–433.

Wade, J., and Wood, B.J. (2001) The Earth's 'missing' niobium may be in the core. Nature, 409, 75–78.

White, J.C., Holt, G.S., Parker, D.F., and Ren, M., (2003) Trace-element partitioning between alkali feldspar and peralkalic quartz trachyte to rhyolite magma. Part I: Systematics of trace-element partitioning. American Mineralogist, 88, 316–329.

White, R.W., Powell, R., Holland, T.J.B., Johnson, T.E., and Green, E.C.R. (2014) New mineral activity–composition relations for thermodynamic calculations in metapelitic systems. Journal Metamorphic Geology, 32, 261–286.

White, R.W., Palin, R.M. and Green, E.C.R. (2017) High‐grade metamorphism and partial melting in Archean composite grey gneiss complexes. Journal of Metamorphic Geology, 35, 181–195.

Whitney, D. L., and Evans, B. W. (2010) Abbreviations for names of rock-forming minerals. American Mineralogist, 95, 185–187.

Willbold, M., and Stracke, A. (2006) Trace element composition of mantle end-members: Implications for recycling of oceanic and upper and lower continental crust. Geochemistry, Geophysics, Geosystem, 7, Q04004.

Xiong, X., Keppler, H., Audétat, A., Ni, H., Sun, W., and Li, Y. (2011) Partitioning of Nb and Ta between rutile and felsic melt and the fractionation of Nb/Ta during partial melting of hydrous metabasalt. Geochimica et Cosmochimica Acta, 75, 1673–1692.

Wang, H.Z., Zhang, H.F., Zhai, M.G., Oliveria, E.P., Ni, Z.Y., Zhao, L., Wu, J.L., and Cui, X.H. (2016) Granulite facies metamorphism and crust melting in the Huai'an terrane at ~ 1.95 Ga, North China Craton: New constraints from geology, zircon U-Pb, Lu-Hf isotope and metamorphic conditions of granulites. Precambrian Research, 286, 126–151.

Wu, J.L., Zhang, H.F., Zhai, M.G., Guo, J.H., Liu, L., Yang, W.Q., Wang, H.Z., Zhao, L., Jia X.L., and Wang ,W. (2016) Discovery of pelitic high-pressure granulite from Manjinggou of the Huai'an Complex, North China Craton: Metamorphic P–T evolution and geological implications. Precambrian Research, 278, 323–336.

Xue, S., Xu, Y., Ling, M.X., Kang, Q.Q., Jiang, X.Y., Sun, S.J., Wu, K., Zhang, Z.K., Luo, Z.M., Liu, Y.H., and Sun, W.D. (2018) Geochemical constraints on genesis of Paleoproterozoic A-type granite in the south margin of North China Craton. Lithos, 304–307, 489–500.

Yakymchuk, C., and Brown, M. (2014) Consequences of open-system melting in tectonics. Journal of Geological Society, London, 171, 21–40.

Yakymchuk, C., Kirkland, C.L., and Clark, C. (2018) Th/U ratios in metamorphic zircon. Journal Metamorphic Geology, 36, 715–737.

Yang, X.Q., Li, Z.L., Wang, H.H., Chen, H.L., Li, Y.Q., and Xiao, W.J. (2015) Petrology and geochemistry of ultrahigh-temperature granulites from the South Altay orogenic belt, northwestern China: Implications for metamorphic evolution and protolith composition. Island Arc, 24, 169–187.

Zack, T., Moraes, R., and Kronz, A. (2004) Temperature dependence of Zr in rutile: empirical calibration of a rutile thermometer. Contributions to Mineralogy and Petrology, 148, 471–488.

Zhang, H.F., Wang, H.Z., Santosh, M., and Zhai, M.G. (2016) Zircon U-Pb ages of Paleoproterozoic mafic granulites from the Huai'an terrane, North China Craton (NCC): Implications for timing of cratonization and crustal evolution history. Precambrian Research, 272, 244–263.

Zhao, G.C., Sun, M., Wilde, S.A., and Li, S.Z. (2005) Late Archean to Paleoproterozoic evolution of the North China Craton: key issues revisited. Precambrian Research, 136, 177–202.

Zong, K.Q., Klemd, R., Yuan, Y., He, Z.Y., Guo, J.L., Shi, X.L., Liu, Y.S., Hu, Z.C., and Zhang, Z.M. (2017) The assembly of Rodinia: The correlation of early Neoproterozoic (ca. 900 Ma) high-grade metamorphism and continental arc formation in the southern Beishan Orogen, southern Central Asian Orogenic Belt (CAOB). Precambrian Research, 290, 32–48.

FIGURE CAPTIONS

FIGURE 1. (a) Tectonic subdivision of the North China Craton showing Precambrian units (Zhao et al., 2005). The red square represents location of Figure 1b. (b) Geological sketch map of the study area (modified after Guo et al., 2001). The ages of different groups and igneous rocks are labeled, of which igneous ages are in black and metamorphic ages are in red.

FIGURE 2. Field photographs of the HT–HP and UHT granulite from the study area. (a-b) HT-HP granulite from the Manjingou area and (c-d) UHT granulite from the Tuguiwula area. (a) Typical HT–HP pelitic granulite (sample 18MJ09) collected from the Manjingou area, northern Trans-North China Orogen. (b) Minor degrees of partial melting in the HT–HP granulite. (c) Typical UHT pelitic granulite (sample 16TG53) from the Tuguiwula area, east Khondalite Belt. (d) Extensive partial melting in the UHT granulite.

FIGURE 3. Photomicrographs of HT–HP granulite sample 18MJ09, shown in plane-polarized light. Panels (a) and (b) show that kyanite occurs as inclusions within garnet rims but is absent in the matrix. Sillimanite is ubiquitous in the matrix. (c) Inclusions of quartz and/or biotite within poikiloblastic garnet cores represent a prograde mineral assemblage (M_0), and rutile occurs as isolated inclusions in garnet (M_1) and in the matrix (M_2). (d) Rutile and biotite inclusions within garnet (M_1) and rutile in the matrix.

FIGURE 4. Sample photomicrographs of UHT granulite, 16TG53, shown in plane-polarized light. (a) Isolated rutile, quartz, and sillimanite inclusions in garnet, representing part of a prograde assemblage (M_0). (b) Isolated rutile inclusion within garnet (M_0) and rutile in the matrix in contact with felsic minerals (M_1). (c) Rutile inclusion in garnet associated with biotite (M_0), rutile in the matrix in contact with felsic minerals, and garnet (M_1). (d) Rutile in the matrix in contact with felsic minerals (M_1) and tiny retrograde rutile along with biotite surrounding garnet (M_2).

FIGURE 5. Bulk-rock composition plots of Nb/Ta vs Nb contents of granulite samples from the study area and other granulite terranes worldwide. Geochemical data summarized from: Trivandrum Block, South India (Nandakumar and Harley, 2019); Ivrea Verbano Zone, north Italy (Ewing et al., 2014); Ulashan-Daqingshan terrane, Khondalite Belt (Cai, 2014); Bhopalpatnam granulite belt, central India (Vansutre et al., 2013); Napier complex, Antarctic (Grew et al., 2006); Altay, northwestern China (Yang et al., 2015); and the Highland complex, Sri Lanka (Table S3). Nb/Ta values of 12.4 in bulk continental crust (BCC) and 19.9 in chondrite are from Rudnick and Gao (2014) and Münker et al. (2003), respectively.

FIGURE 6. (a) Plots of bulk-rock Nb/Ta vs A/CNK (molar $Al_2O_3/(Na_2O+K_2O+CaO)$) from muscovite-bearing peraluminous granites worldwide (Ballouard et al., 2020) and leucosomes of UHT granulites from the Khondalite Belt. Highly differentiated muscovite-bearing peraluminous granites with Nb/Ta < 5 suspected to have experienced significant magmatic-hydrothermal alteration were ruled out from the compilation. (b) Plots of Nb/Ta vs A/CNK for calculated melts.

FIGURE 7. Plots of Nb/Ta vs Zr concentration of rutile (LA-ICP-MS data) in (a) HT-HP granulite sample 18MJ09 from Trans-North China Orogen and (b) UHT samples 16TG53 from Khondalite Belt.

FIGURE 8. Mineral proportion vs. metapelite temperature during isobaric heating at 0.8 GPa. Mineral abbreviations: Qz: quartz; Sill: sillimanite; Ky: kyanite; Rt: rutile; Ilm: ilmenite; Bt: biotite; Kfs: K-feldspar; Ms: muscovite; Pl: plagioclase; Grt: garnet.

FIGURE 9. Calculated Nb/Ta ratios vs. temperature for petrological modeling. (a) Nb/Ta evolution of extracted melts and residue during isobaric heating at 0.8 GPa. (b) Nb/Ta evolution of extracted melts and residue along a 775 °C/GPa geotherm. (c) Nb/Ta evolution of extracted melts and residues along a 550 °C/GPa geotherm.

FIGURE 10. Nb/Ta frequency plots for typical pelitic granulites worldwide. Geochemical data are the same as shown in Fig. 5.

FIGURE 11. Niobium and Ta concentrations in S-type granite, A2-type granite, leucosome in UHT terrane (this study), and calculated melts in equilibrium with rutile. Granite data are from Ballouard et al. (2020).

This is the peer-reviewed, final accepted version for American Mineralogist, published by the Mineralogical Society of America.
The published version is subject to change. Cite as Authors (Year) Title. American Mineralogist, in press.
DOI: https://doi.org/10.2138/am-2022-8260. http://www.minsocam.org/

FIGURE S1. (a) *P–T* mosaic pseudosection panels of a metapelite in an open system along isobaric heating at 0.8 GPa (green arrow), contoured with isopleths of mol. % melt (black dash line and number within square symbols). (b) Mineral proportion evolution vs. temperature.

FIGURE S2. (a) *P–T* mosaic pseudosection panels for a metapelite experiencing open-system metamorphism along a 775 °C/GPa geotherm (green arrow), contoured with isopleths of mol. % melt. (b) Mineral proportion evolution vs. temperature.

FIGURE S3. (a) *P–T* mosaic pseudosection panels for a metapelite experiencing open-system metamorphism along a 550 °C/GPa geotherm (green arrow), contoured with isopleths of mol. % melt. (b) Mineral proportion evolution vs. temperature.

FIGURE S4. Tectonic subdivision of Sri Lanka metamorphic basement modified after Cooray (1994). Samplesof the studied UHT metamorphic rocks (18HC05, 18HC06, 18KC21, 18KC22-2, 18KC23, 18KC96-2) are shown as a red star. Am: amphibolite facies; Gn: granulite facies.

FIGURE S5. Bulk-rock composition plots of Nb/Ta vs Ta contents of granulite samples from the study area and other granulite terranes worldwide. Geochemical data summarized from: Trivandrum Block, South India (Nandakumar and Harley, 2019); Ivrea Verbano Zone, north Italy (Ewing et al., 2014); Ulashan-Daqingshan terrane, Khondalite Belt (Cai, 2014); Bhopalpatnam granulite belt, central India (Vansutre et al., 2013); Napier complex, Antarctic (Grew et al., 2006); Altay, northwestern China (Yang et al., 2015); and the Highland complex,

DOI: https://doi.org/10.2138/am-2022-8260. http://www.minsocam.org/

Sri Lanka (Table S3). Nb/Ta values of 12.4 in bulk continental crust (BCC) and 19.9 in chondrite are from Rudnick and Gao (2014) and Münker et al. (2003), respectively.

Table 1 Partition coefficients used in trace element modeling

Mineral	D_{Nb} Mean	D_{Ta} Mean	References
Kfs	0.03	0.04	1-5
Pl	0.03	0.04	2-3
Grt	0.02	0.04	2,6-8
Bt	3.89	1.53	1-3,9
Ms	3.5	0.4	10
Rt	159.5(51.1)	196(113)	11-12
Ilm	0.715	1.115	13
Zrn	0.46	0.64	2
Ap	0.012	0.012	2
Mnz	0.03	0.06	2

1: Nash and Crecraft (1985); 2: Acosta-Vigil et al. (2010); 3: Fedele et al. (2015); 4: Sweeney et al. (1995); 5: White et al. (2003); 6: Klemme et al. (2002); 7: Qian and Hermann (2013); 8: Fulmer et al. (2010); 9: Stepanov and Hermann (2013); 10: Raimbault and Burnol (1998); 11: Xiong et al. (2011); 12: Klemme et al. (2005); 13: Klemme et al. (2006). Note that D_{Nb} and D_{Ta} of rutile from Xiong et al. (2011)[11] were averaged values at 850 °C used for modeling of biotite dehydration melting, whereas those from Klemme (2005)[12] were used for modeling at anhydrous condition. Mineral abbreviations from Whitney and Evans (2010)

Figure 1

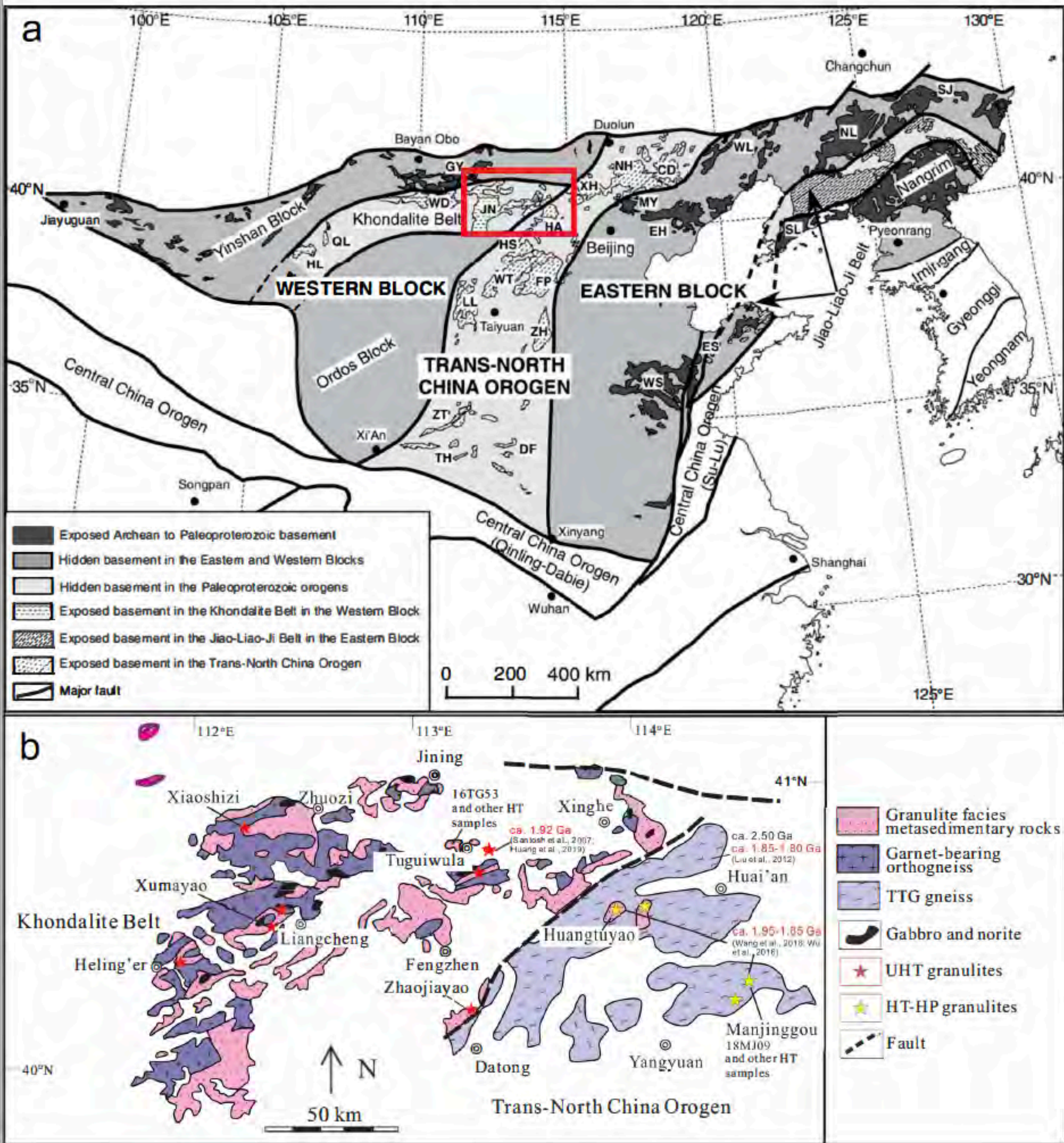

a
100°E
105°E
110°E
115°E
120°E
125°E
130°E
40°N
35°N
30°N
125°E
Changchun
SJ
NL
Duolun
Bayan Obo
GY
NH
CD
WL
XH
MY
Nangrim
JN
WD
HA
Khondalite Belt
Jiayuguan
Yinshan Block
QL
HL
HS
Beijing
EH
SL
Pyeonrang
Imjingang
Gyeonggi
WESTERN BLOCK
WT
FP
EASTERN BLOCK
Jiao-Liao-Ji Belt
LL
Taiyuan
ZH
Ordos Block
TRANS-NORTH CHINA OROGEN
ES
WS
Yeongnam
Central China Orogen
ZT
Xi'An
TH
DF
Central China Orogen (Su-Lu)
Songpan
Central China Orogen (Qinling-Dabie)
Xinyang
Shanghai
Wuhan
Exposed Archean to Paleoproterozoic basement
Hidden basement in the Eastern and Western Blocks
Hidden basement in the Paleoproterozoic orogens
Exposed basement in the Khondalite Belt in the Western Block
Exposed basement in the Jiao-Liao-Ji Belt in the Eastern Block
Exposed basement in the Trans-North China Orogen
Major fault
0 200 400 km
b
112°E
113°E
114°E
41°N
40°N
Jining
Xiaoshizi
Zhuozi
16TG53 and other HT samples
ca. 1.92 Ga
Xinghe
Tuguiwula
ca. 2.50 Ga
ca. 1.85-1.80 Ga
Huai'an
Xumayao
Khondalite Belt
Liangcheng
Huangtuyao
ca. 1.95-1.85 Ga
Heling'er
Fengzhen
Zhaojiayao
Manjinggou
18MJ09 and other HT samples
N
Datong
Yangyuan
50 km
Trans-North China Orogen
Granulite facies metasedimentary rocks
Garnet-bearing orthogneiss
TTG gneiss
Gabbro and norite
UHT granulites
HT-HP granulites
Fault

Figure 2

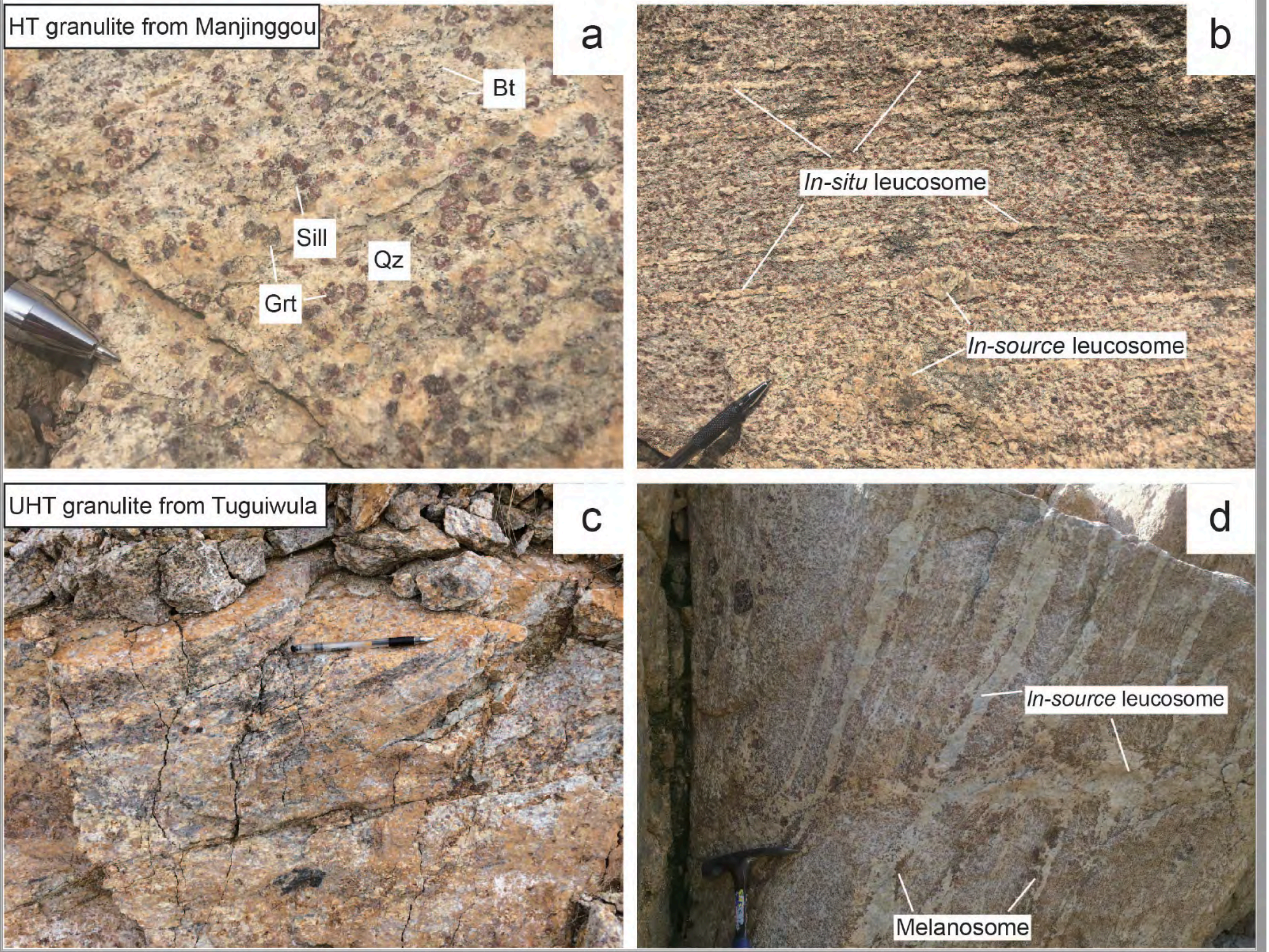

HT granulite from Manjinggou
a
Bt
Sill
Qz
Grt
b
In-situ leucosome
In-source leucosome
UHT granulite from Tuguiwula
c
d
In-source leucosome
Melanosome

Figure 3

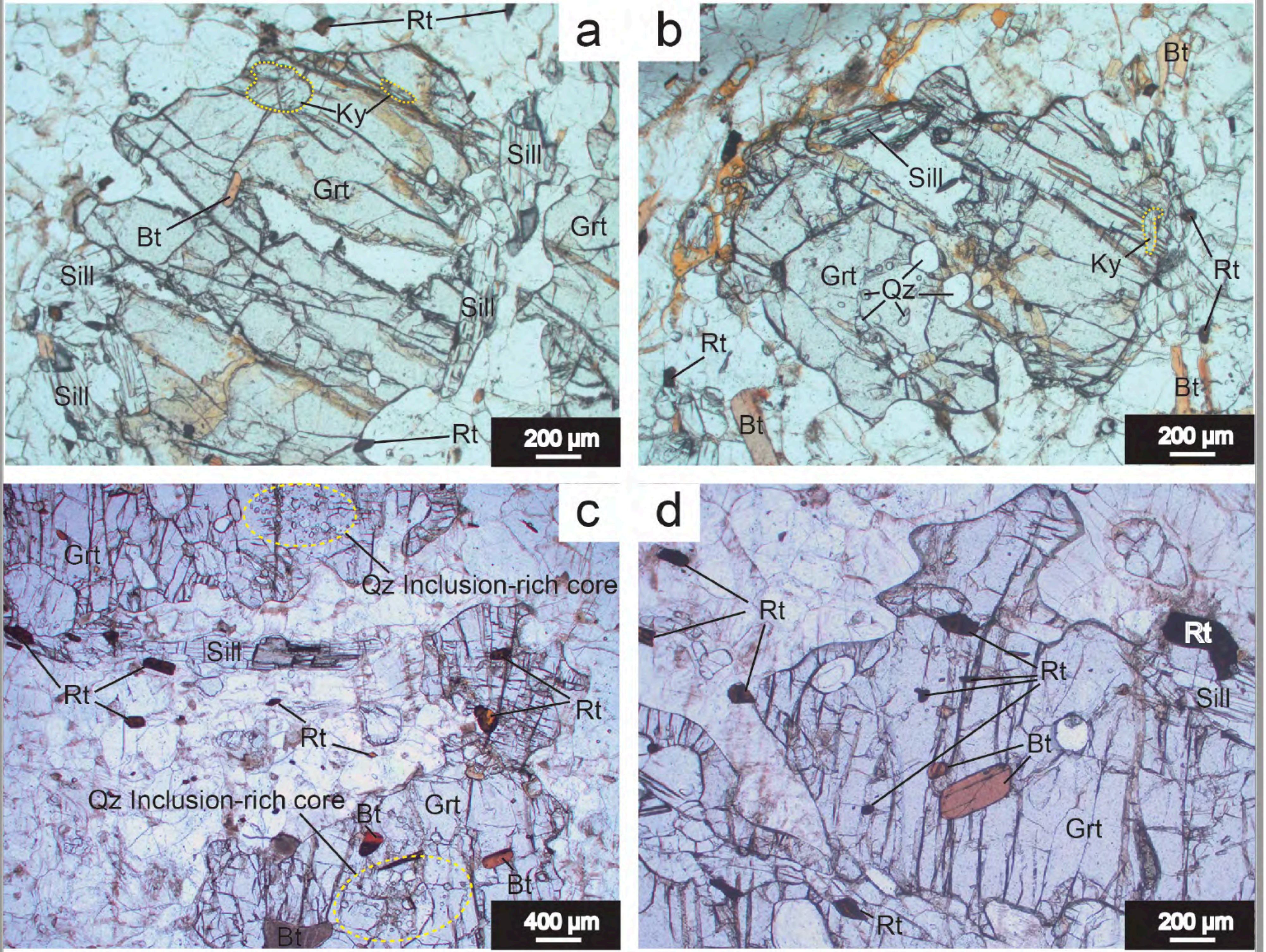

a
Rt
Ky
Sill
Grt
Bt
Sill
Sill
Grt
Sill
Rt
200 µm
b
Bt
Sill
Ky
Rt
Grt
Qz
Rt
Bt
Bt
200 µm
c
Grt
Qz Inclusion-rich core
Sill
Rt
Rt
Rt
Qz Inclusion-rich core
Bt
Grt
Bt
Bt
400 µm
d
Rt
Rt
Rt
Sill
Bt
Grt
Rt
200 µm

Figure 4

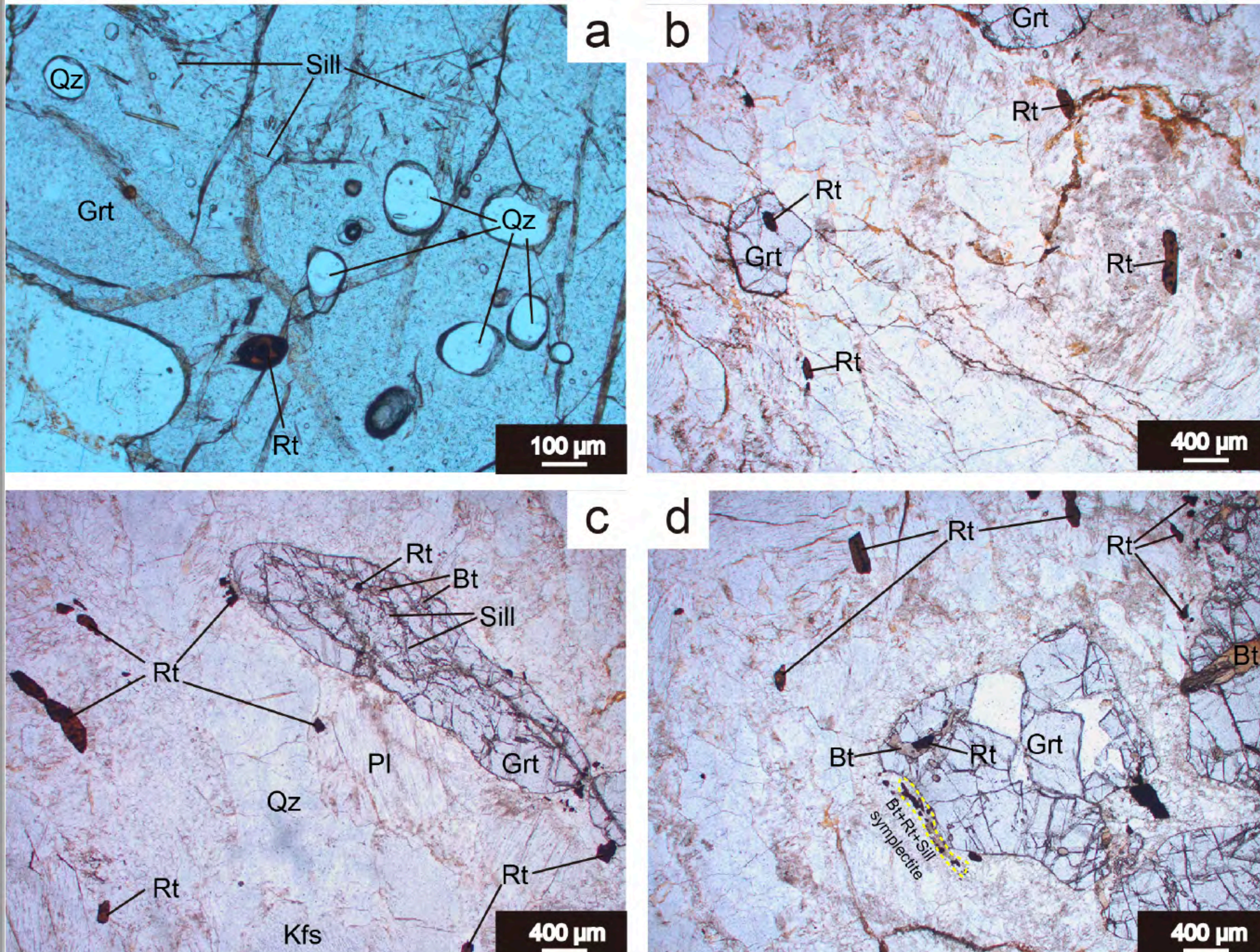

a
Qz
Sill
Grt
Qz
Rt
100 μm
b
Grt
Rt
Rt
Grt
Rt
Rt
400 μm
c
Rt
Bt
Sill
Rt
Pl
Grt
Qz
Rt
Rt
Kfs
400 μm
d
Rt
Rt
Bt
Bt
Rt
Grt
Bt+Rt+Sill
symplectite
400 μm

Figure 5

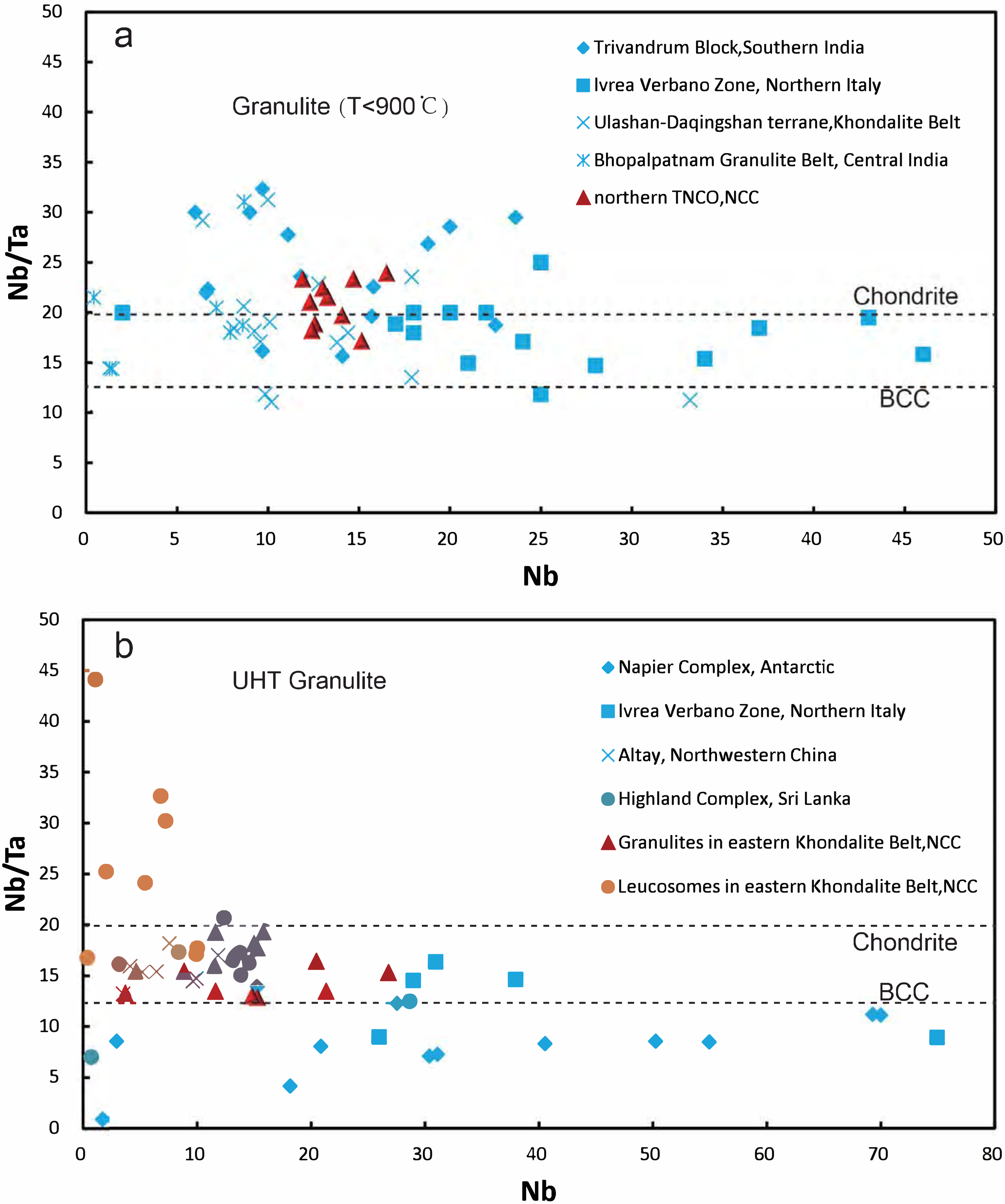

a
Granulite（T<900℃）
Trivandrum Block,Southern India
Ivrea Verbano Zone, Northern Italy
Ulashan-Daqingshan terrane,Khondalite Belt
Bhopalpatnam Granulite Belt, Central India
northern TNCO,NCC
Chondrite
BCC
Nb/Ta
Nb
b
UHT Granulite
Napier Complex, Antarctic
Ivrea Verbano Zone, Northern Italy
Altay, Northwestern China
Highland Complex, Sri Lanka
Granulites in eastern Khondalite Belt,NCC
Leucosomes in eastern Khondalite Belt,NCC
Chondrite
BCC
Nb/Ta
Nb

Figure 6

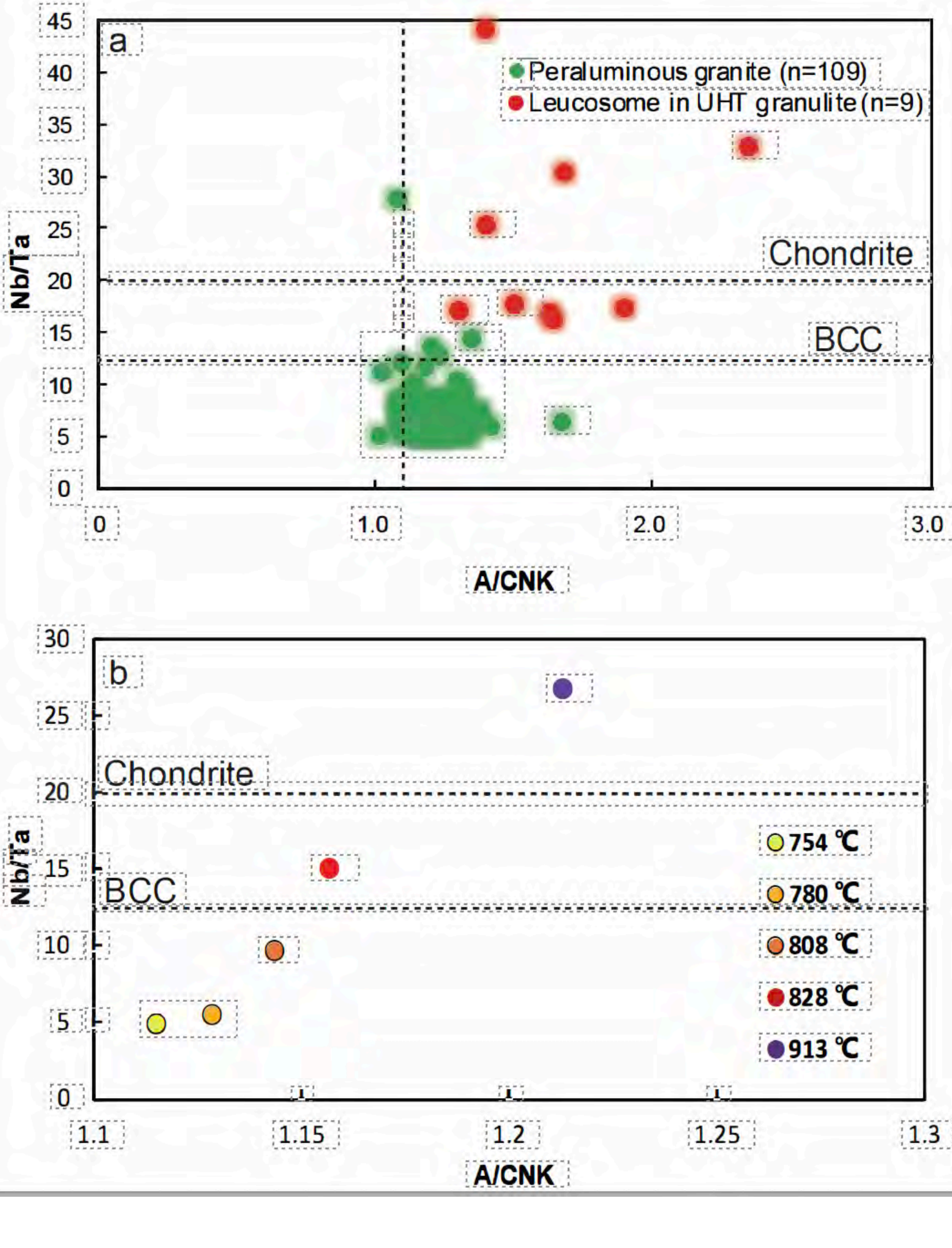
a
Peraluminous granite (n=109)
Leucosome in UHT granulite (n=9)
Chondrite
BCC
Nb/Ta
A/CNK
0
5
10
15
20
25
30
35
40
45
0
1.0
2.0
3.0
b
Chondrite
BCC
754 ℃
780 ℃
808 ℃
828 ℃
913 ℃
Nb/Ta
A/CNK
0
5
10
15
20
25
30
1.1
1.15
1.2
1.25
1.3

Figure 7

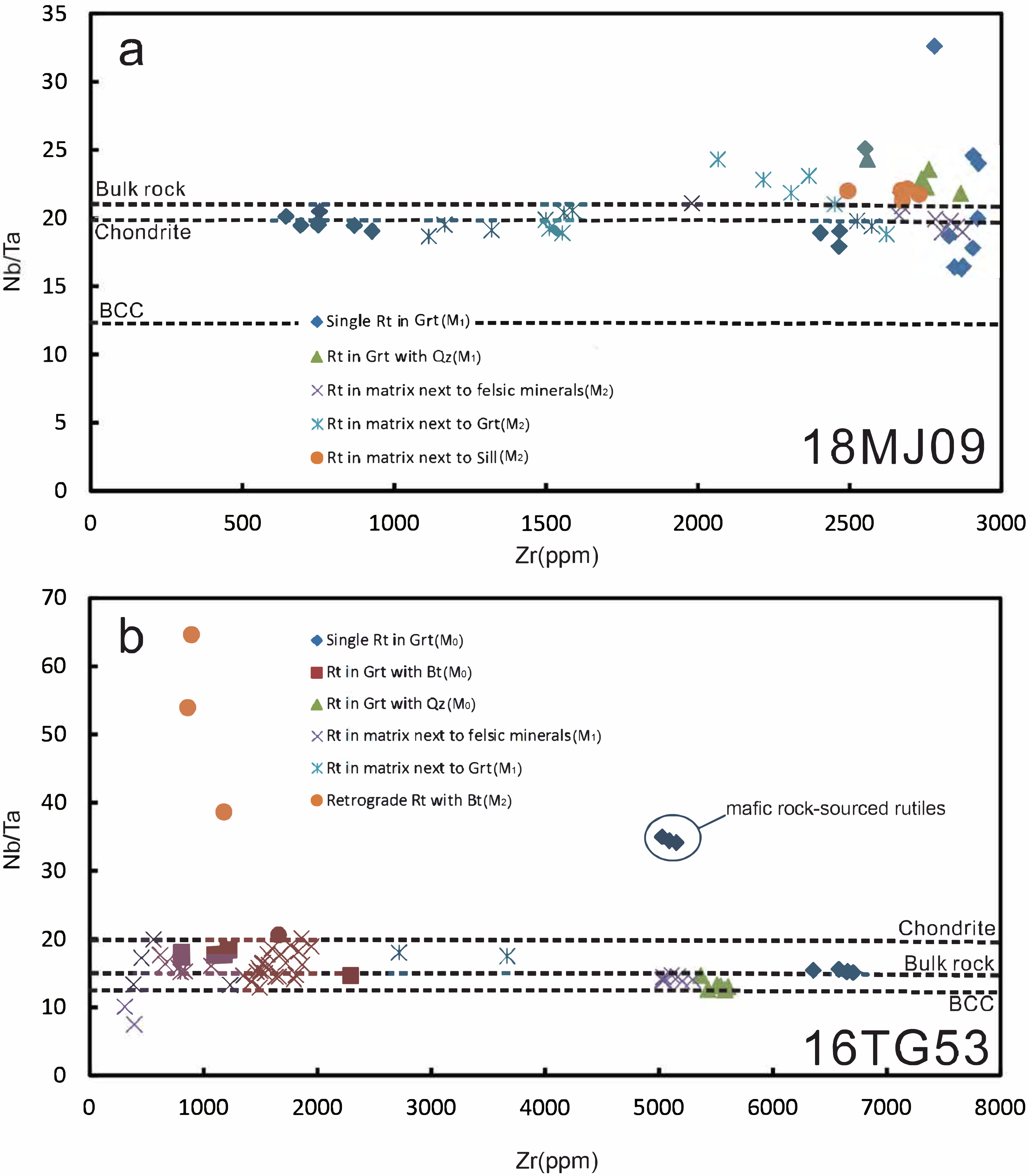
a
18MJ09
Bulk rock
Chondrite
BCC
Single Rt in Grt(M1)
Rt in Grt with Qz(M1)
Rt in matrix next to felsic minerals(M2)
Rt in matrix next to Grt(M2)
Rt in matrix next to Sill(M2)
Nb/Ta
Zr(ppm)
0
5
10
15
20
25
30
35
0
500
1000
1500
2000
2500
3000
b
16TG53
Single Rt in Grt(M0)
Rt in Grt with Bt(M0)
Rt in Grt with Qz(M0)
Rt in matrix next to felsic minerals(M1)
Rt in matrix next to Grt(M1)
Retrograde Rt with Bt(M2)
mafic rock-sourced rutiles
Chondrite
Bulk rock
BCC
Nb/Ta
Zr(ppm)
0
10
20
30
40
50
60
70
0
1000
2000
3000
4000
5000
6000
7000
8000

Figure 8

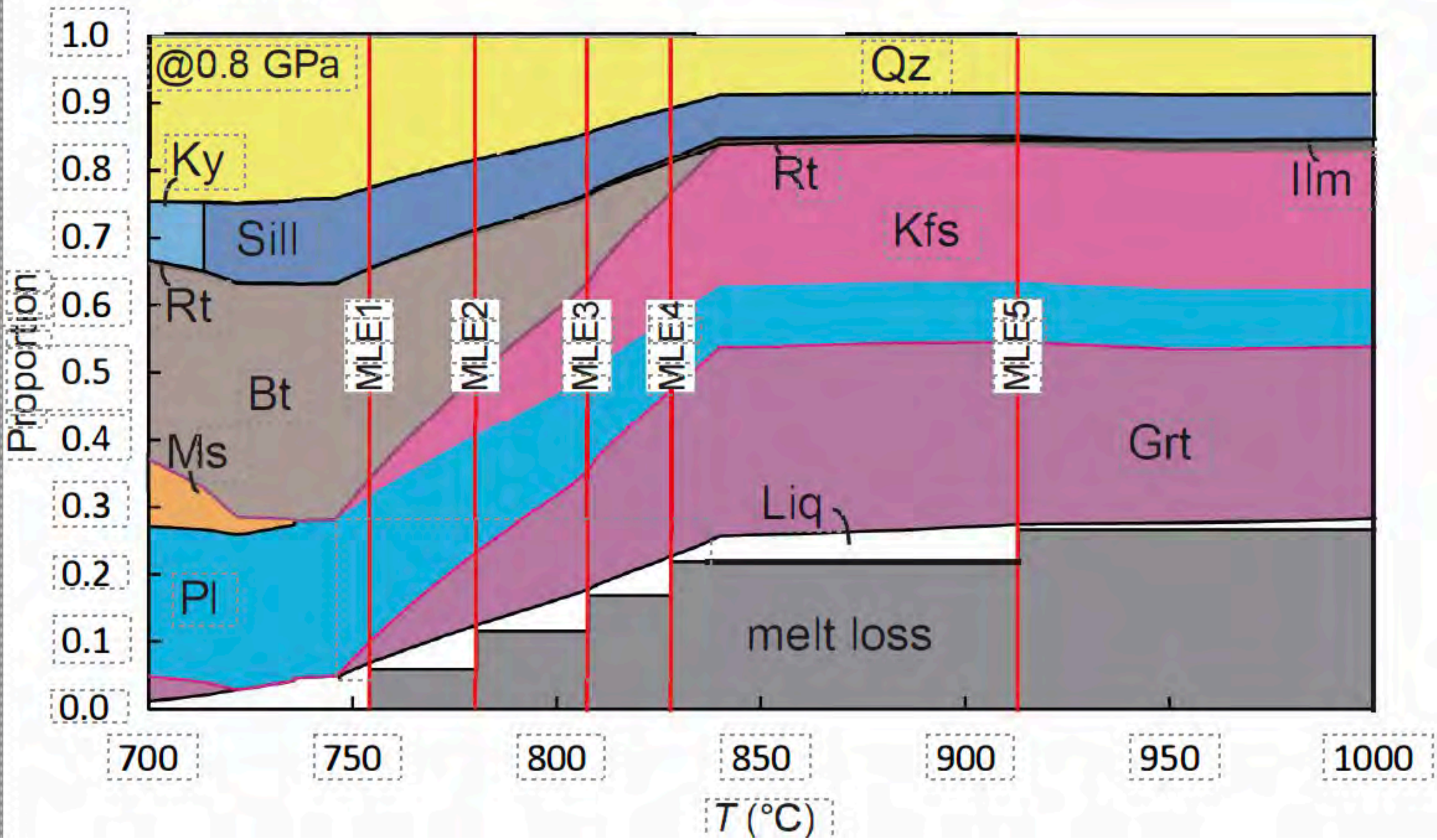

@0.8 GPa
Qz
Ky
Sill
Rt
Bt
Ms
Pl
Kfs
Rt
Ilm
Grt
Liq
melt loss
MLE1
MLE2
MLE3
MLE4
MLE5
Proportion
1.0
0.9
0.8
0.7
0.6
0.5
0.4
0.3
0.2
0.1
0.0
700
750
800
850
900
950
1000
T (°C)

Figure 9

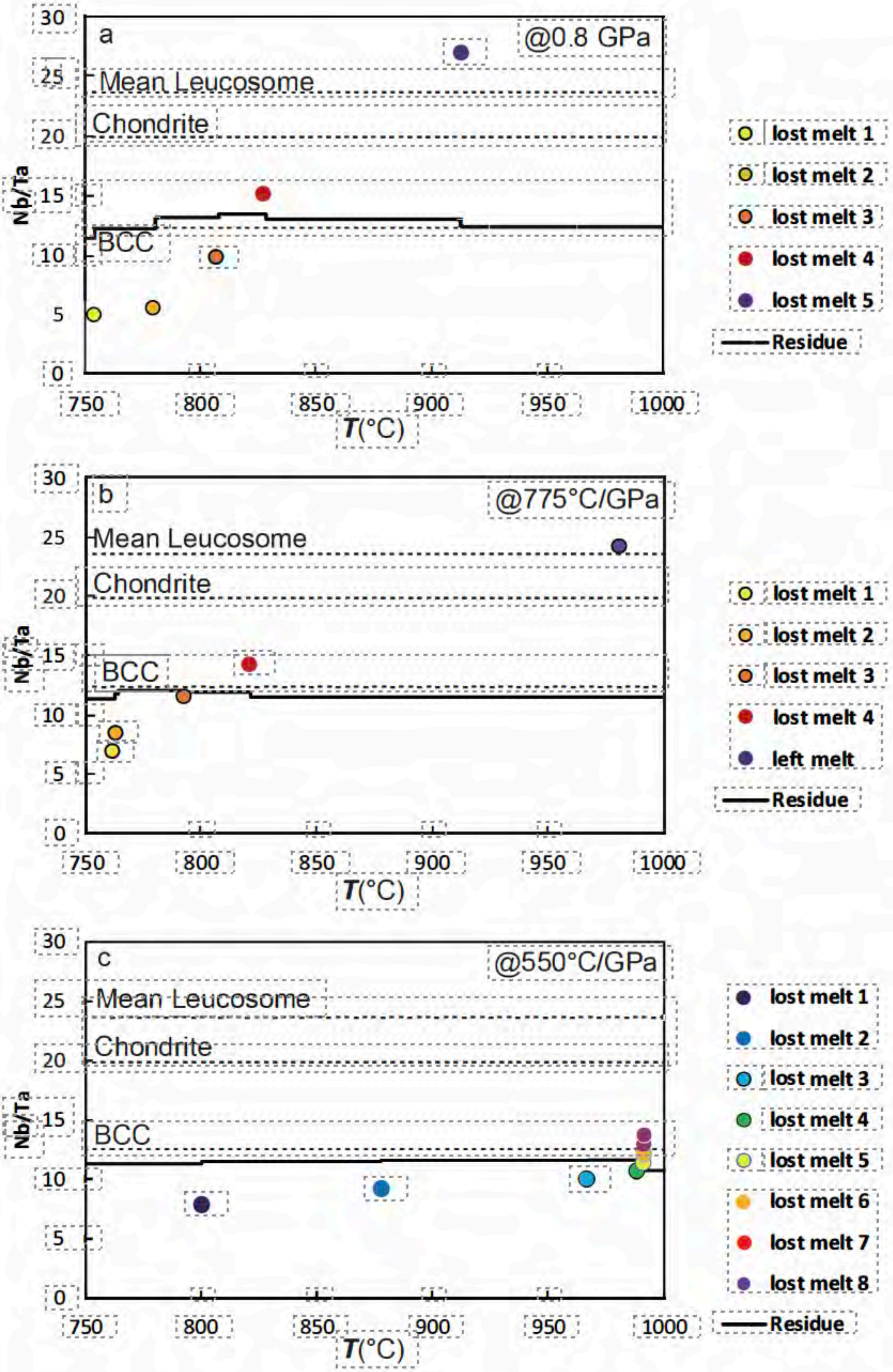
a
@0.8 GPa
Mean Leucosome
Chondrite
BCC
Nb/Ta
T(°C)
lost melt 1
lost melt 2
lost melt 3
lost melt 4
lost melt 5
Residue
b
@775°C/GPa
Mean Leucosome
Chondrite
BCC
Nb/Ta
T(°C)
lost melt 1
lost melt 2
lost melt 3
lost melt 4
left melt
Residue
c
@550°C/GPa
Mean Leucosome
Chondrite
BCC
Nb/Ta
T(°C)
lost melt 1
lost melt 2
lost melt 3
lost melt 4
lost melt 5
lost melt 6
lost melt 7
lost melt 8
Residue

Figure 10

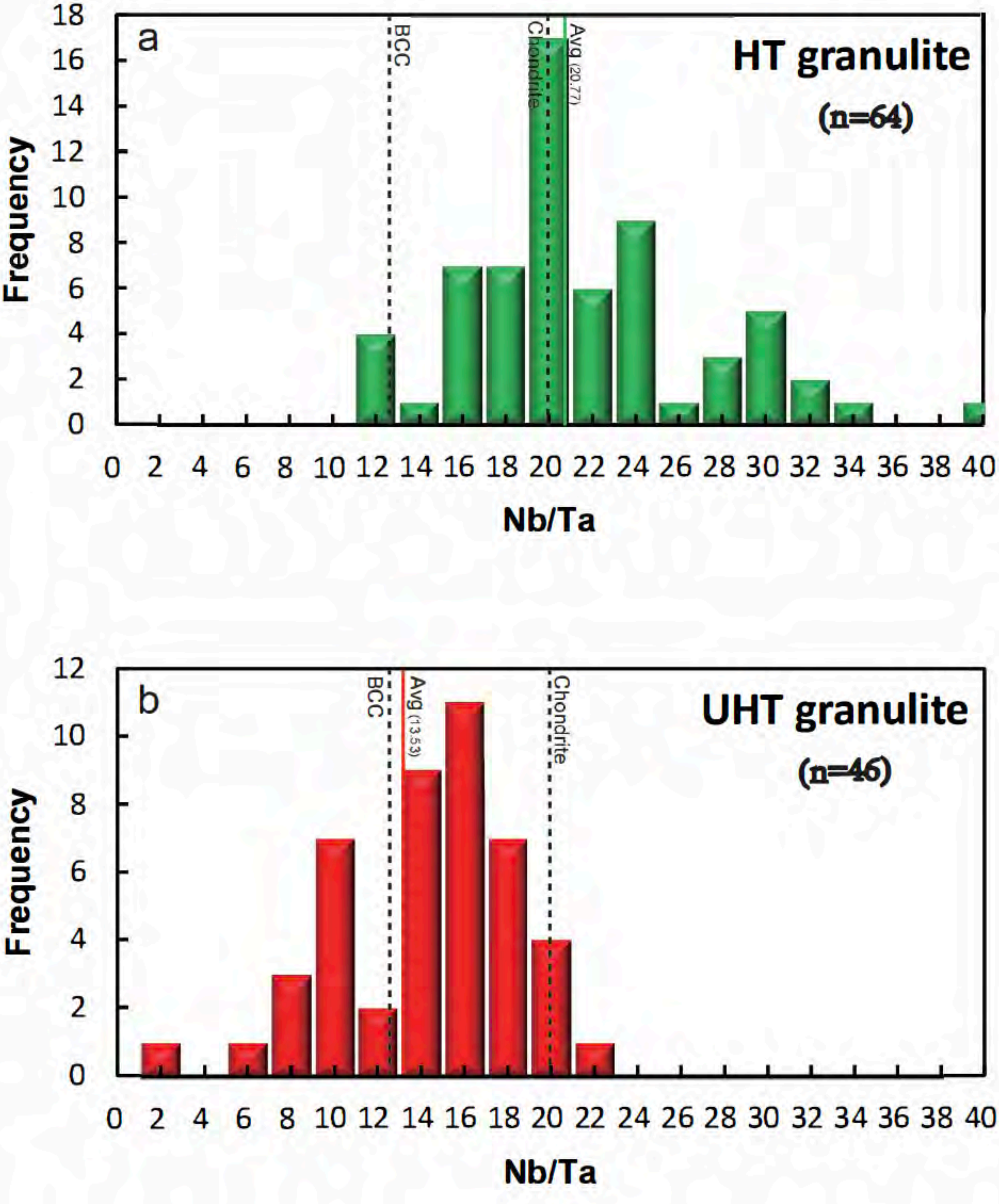

a
HT granulite
(n=64)
BCC
Chondrite
Avg (20.77)
Frequency
Nb/Ta
b
UHT granulite
(n=46)
BCC
Avg (13.53)
Chondrite
Frequency
Nb/Ta

Figure 11

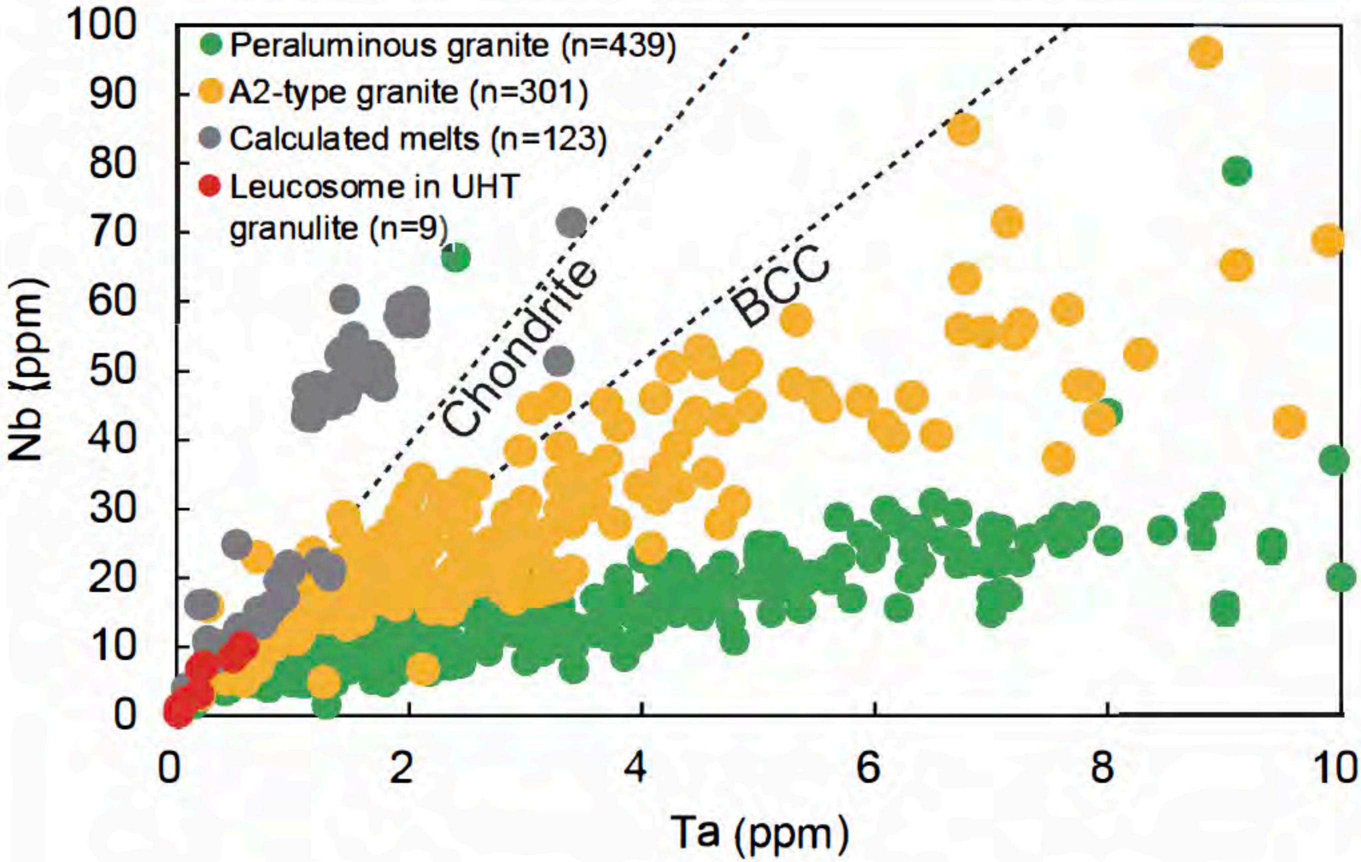
100
90
80
70
60
50
40
30
20
10
0
Nb (ppm)
0
2
4
6
8
10
Ta (ppm)
Peraluminous granite (n=439)
A2-type granite (n=301)
Calculated melts (n=123)
Leucosome in UHT granulite (n=9)
Chondrite
BCC